IMMUNOLOGY

TOP CAR with TMIGD2 as a safe and effective costimulatory domain in CAR cells treating human solid tumors

Christopher D. Nishimura[1,2], Devin Corrigan[1,2], Xiang Yu Zheng[3], Phillip M. Galbo Jr.[1,3], Shan Wang[1], Yao Liu[1], Yao Wei[1], Linna Suo[1], Wei Cui[1], Nadia Mercado[4], Deyou Zheng[3], Cheng Cheng Zhang[5], Xingxing Zang[1,2,6,7,8]*

Chimeric antigen receptor (CAR)–T cell therapy shows impressive efficacy treating hematologic malignancies but requires further optimization in solid tumors. Here, we developed a TMIGD2 optimized potent/persistent (TOP) CAR that incorporated the costimulatory domain of TMIGD2, a T and NK cell costimulator, and monoclonal antibodies targeting the IgV domain of B7-H3, an immune checkpoint expressed on solid tumors and tumor vasculature. Comparing second- and third-generation B7-H3 CARs containing TMIGD2, CD28, and/or 4-1BB costimulatory domains revealed superior antitumor responses in B7-H3.TMIGD2 and B7-H3.CD28.4-1BB CAR-T cells in vitro. Comparing these two constructs using in vivo orthotopic human cancer models demonstrated that B7-H3.TMIGD2 CAR-T cells had equivalent or superior antitumor activity, survival, expansion, and persistence. Mechanistically, B7-H3.TMIGD2 CAR-T cells maintained mitochondrial metabolism; produced less cytokines; and established fewer exhausted cells, more central memory cells, and a larger CD8/CD4 T cell ratio. These studies demonstrate that the TOP CAR with TMIGD2 costimulation offered distinct benefits from CD28.41BB costimulation and is effective against solid tumors.

INTRODUCTION

Chimeric antigen receptor (CAR)–T cell therapy has revolutionized the treatment of hematologic malignancies, demonstrating impressive antitumor responses and improved survival outcomes (1–3). Consequently, there are now six Food and Drug Administration (FDA)–approved CAR-T cell therapies targeting various hematologic malignancies (4). Such successes have prompted substantial work to bring CAR-T cell therapy to the solid tumor realm. However, clinical data have thus far shown that CAR-T cells are largely ineffective with only modest responses across multiple tumor types (5–8). Thus, further engineering of CAR design is necessary.

The choice of costimulatory domain plays a major role in shaping the functional characteristics of CAR-T cells (9). For example, CAR-T cells incorporating a 4-1BB costimulatory domain show increased persistence (10, 11), decreased cytokine release (11, 12), and enrichment of central memory cells (13, 14) compared to CAR-T cells with a CD28 costimulatory domain. Such differences may, in part, underlie clinical outcomes. Although it is challenging to compare different clinical trial results due to variations in CAR and trial design, studies with direct comparisons of these costimulatory domains in CD19 CARs suggest that 4-1BB–based CARs mediate safer or superior clinical outcomes compared to their CD28-based counterparts in hematologic malignancies (11, 15). Given the modest clinical trial responses in solid tumors, further testing of alternative costimulatory domains that can impart more favorable CAR-T cell phenotypes represents a powerful approach to improve CAR-T cell therapy targeting solid tumors.

We and others have previously described the T and NK cell costimulatory protein Transmembrane and immunoglobulin domain–containing 2 [TMIGD2/Immunoglobulin and proline-rich receptor-1 (IGPR-1)/Cluster of differentiation 28 homolog (CD28H)] that mediates costimulation via binding to human endogenous retrovirus-H long terminal repeat–associating 2 (HHLA2) (16–20). Intriguingly, TMIGD2 expression irreversibly decreases upon T cell activation and differentiation, and TMIGD2⁻ T cells exhibit detrimental phenotypic changes, including decreased proliferation and the acquisition of a senescent phenotype (20). Furthermore, TMIGD2⁻ T cells exhibit alterations in cytokine expression (21, 22). These findings suggest that maintaining TMIGD2 signaling may be an effective strategy to support CAR-T cell effector function by preventing senescence, decreased proliferation, and alteration of cytokine release.

We therefore generated and tested a TMIGD2 optimized potent/persistent (TOP) CAR with a TMIGD2 costimulatory domain in CAR-T cells targeting B7-H3, an immune checkpoint broadly expressed on most solid tumors and tumor vasculature, but with limited expression on healthy tissue (23). We hypothesized that this combination would allow us to target a wide range of solid tumors and tumor vasculature, block the inhibitory interaction of B7-H3 on T cells, and prevent the detrimental effects caused by the loss of TMIGD2 signaling. In vitro comparison of second- and third-generation B7-H3 CARs incorporating CD28, TMIGD2, and/or 4-1BB costimulatory domains revealed that B7-H3.TMIGD2 and B7-H3.CD28.4-1BB CAR-T cells mediated superior antitumor responses. Further in vivo comparisons with these two CAR-T cells using three solid tumor models showed that the B7-H3.TMIGD2 CAR-T cells were as good or better than B7-H3.CD28.4-1BB CARs

[1]Department of Microbiology and Immunology, Albert Einstein College of Medicine, Bronx, NY 10461, USA. [2]Institute for Immunotherapy of Cancer, Albert Einstein College of Medicine, Bronx, NY 10461, USA. [3]Department of Genetics, Albert Einstein College of Medicine, Bronx, NY 10461, USA. [4]Department of Biostatistics, Brown University School of Public Health, Providence, RI 02903, USA. [5]Department of Physiology, University of Texas Southwestern Medical Center, Dallas, TX 75390, USA. [6]Department of Oncology, Albert Einstein College of Medicine, Bronx, NY 10461, USA. [7]Department of Medicine, Albert Einstein College of Medicine, Bronx, NY 10461, USA. [8]Department of Urology, Albert Einstein College of Medicine, Bronx, NY 10461, USA.

*Corresponding author. Email: xingxing.zang@einsteinmed.edu

with regard to antitumor responses, survival outcomes, expansion, and persistence. Mechanistically, TMIGD2 costimulation imparted changes in metabolic, exhaustion, memory, and CD8/CD4 populations. Together, these data demonstrate that our B7-H3.TMIGD2 CAR-T cell is a promising therapeutic strategy to target human solid tumors.

RESULTS

Generation and characterization of monoclonal antibodies against the IgV functional domain of B7-H3

To construct our B7-H3 CAR, we first generated a panel of anti–B7-H3 monoclonal antibodies (mAbs). We and others demonstrate that the immunoglobulin V (IgV) domain is the functional domain of B7-H3 (*24*), so we generated all mAbs against the IgV domain. We obtained nine anti–B7-H3 mAb clones denoted as 8B12, 24D12, 1G5, 15F9, 1C6, 12B4, 16E6, 8B4, and 19C9 that did not bind all other B7 family members and bound to both mouse and human B7-H3 at affinities ranging from 0.3 to 28.75 nM using biolayer interferometry (BLI) (Fig. 1A). By flow cytometry, we confirmed the binding of these mAbs to mouse and human B7-H3 stably expressed on 3T3 cells (Fig. 1B). We additionally tested whether these anti–B7-H3 mAbs could bind to nonhuman primate cynomolgus B7-H3. All anti–B7-H3 mAbs were able to detect cynomolgus B7-H3 stably expressed on 3T3 cells by flow cytometry (Fig. 1C). Thus, our anti–B7-H3 mAbs were able to recognize human, mouse, and cynomolgus B7-H3.

In vitro comparison of various anti–B7-H3 CAR-T cells

Using a single-chain variable fragment (scFv) derived from anti–B7-H3 mAb clone 8B12, we constructed anti–B7-H3 CARs by sequentially linking the scFv to a human CD8α hinge and transmembrane (H/TM) domain, the intracellular domain of various costimulatory proteins (described below), and the intracellular domain of CD3ζ.
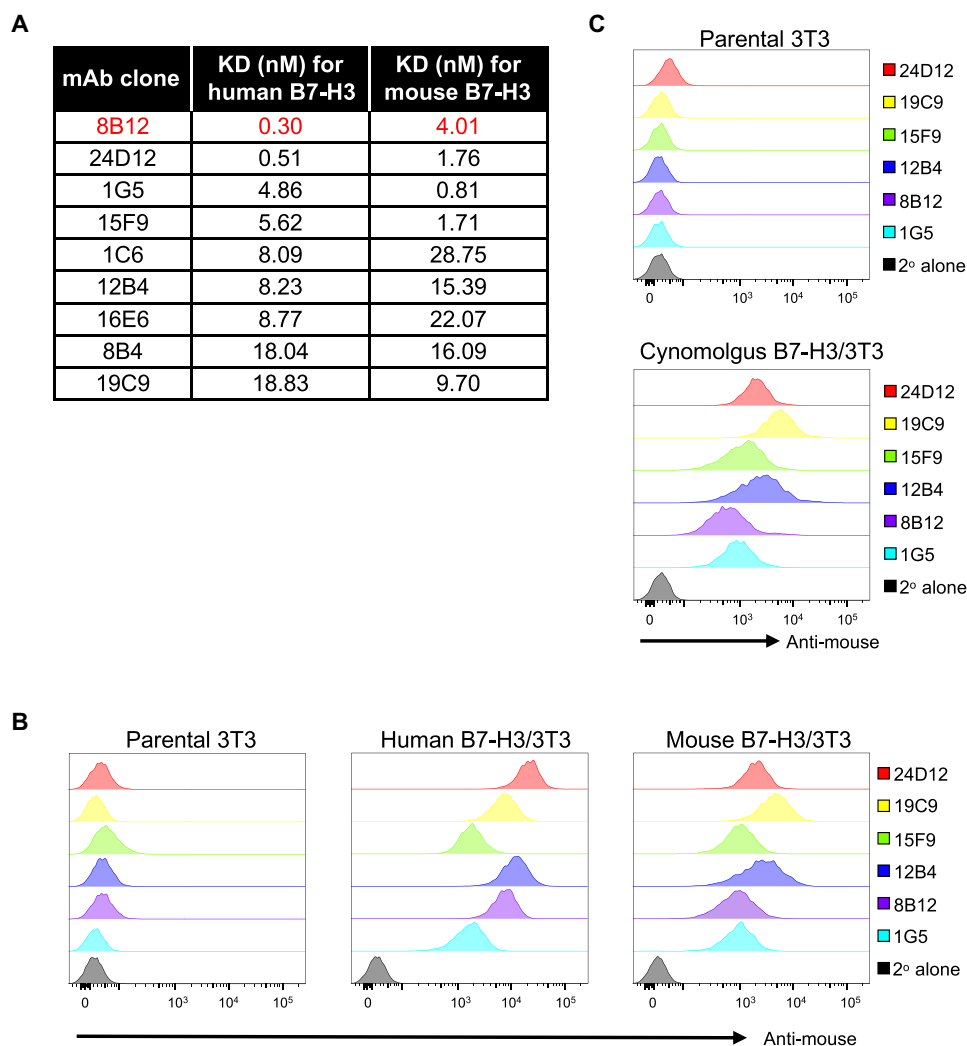
mAb clone	KD (nM) for human B7-H3	KD (nM) for mouse B7-H3
8B12	0.30	4.01
24D12	0.51	1.76
1G5	4.86	0.81
15F9	5.62	1.71
1C6	8.09	28.75
12B4	8.23	15.39
16E6	8.77	22.07
8B4	18.04	16.09
19C9	18.83	9.70

Fig. 1. Characterization of anti–B7-H3 mAbs. (**A**) KD of anti–B7-H3 mAbs against human and mouse B7-H3 as determined by biolayer interferometry (BLI). Red text indicates mAb clone chosen to generate the B7-H3 scFv. (**B**) Histograms depicting anti–B7-H3 mAb binding to parental 3T3 cells or 3T3 cells expressing either mouse or human B7-H3. (**C**) Histograms depicting anti–B7-H3 mAb binding to parental 3T3 cells or 3T3 cells expressing cynomolgus B7-H3. Histograms depicted in (B) and (C) are representative of two independent experiments.

After the CD3ζ sequence, we included a self-cleaving P2A peptide and a truncated human epidermal growth factor receptor (hEGFRt) (Fig. 2A). The hEGFRt protein was modified by removing two of four extracellular domains and all intracellular domains to prevent ligand binding and signaling as previously described (25). As it can still be recognized by anti-EGFR antibodies, hEGFRt functioned as a marker of transduction efficiency in our current study and a safety switch in future clinical trials. We used the following costimulatory domains in our CAR constructs: CD28 (B7-H3.28.ζ CAR), 4-1BB (B7-H3.BB.ζ CAR), TMIGD2 (B7-H3.TMI.ζ CAR), CD28.4-1BB (B7-H3.28.BB.ζ CAR), or TMIGD2.4-1BB (B7-H3.TMI.BB.ζ CAR). An anti-CD19 CAR was similarly generated from a commercially available construct using an anti-CD19 scFv and with the CD28.4-1BB costimulatory domains to serve as an irrelevant target control (CD19.28.BB.ζ) (Fig. 2A). On primary human T cells, all CAR constructs were efficiently expressed with transduction efficiencies regularly greater than 85% CAR$^+$ as determined by expression of the hEGFRt protein, and there was no difference in memory phenotype or expansion between the CAR-T cell constructs (fig. S1).

We next tested the in vitro antitumor activity of our B7-H3 CAR-T cells against multiple tumor types that were B7-H3$^+$ by flow cytometry (fig. S2). In these experiments, we lowered CAR-T cell transduction efficiency to 50% using non-transduced T cells to better reflect transduction efficiencies seen in clinical trials (26, 27). U118 glioblastoma (GBM) and HCC827 lung cancer cell lines were stably transfected with a plasmid expressing Luciferase and tdTomato (-Luc) proteins to allow for tumor cell discrimination. B7-H3.TMI.ζ and B7-H3.28.BB.ζ CAR-T cells demonstrated tumor cell killing against U118-Luc cells (Fig. 2B). B7-H3.28.ζ, B7-H3.TMI.ζ, and B7-H3.28.BB.ζ CAR-T cells demonstrated tumor cell killing against HCC827-Luc cells (Fig. 2C). To confirm that our CARs were effective against nonsolid tumors as well, we examined whether our CAR-T cells could target the THP-1 acute monocytic leukemia (AML) cell line. B7-H3.TMI.ζ, B7-H3.28.BB.ζ, and B7-H3.TMI.BB.ζ CAR-T cells showed significant tumor cell killing against THP-1 cells (Fig. 2D). Although donor-to-donor variability was high, we consistently found that B7-H3.TMI.ζ and B7-H3.28.BB.ζ CAR-T cells elicited antitumor responses across all cell lines tested. Thus, these two CARs represented our lead candidates and were used in all future experiments.

We then sought to examine whether there were differences in the kinetics of tumor cell killing between these two CARs. We performed a time-lapse imaging cytotoxicity assay by repeatedly imaging U118-Luc or HCC827-Luc tumor cells alone or cocultured with B7-H3.TMI.ζ, B7-H3.28.BB.ζ, or CD19.28.BB.ζ CAR-T cells. Live tumor cell growth was tracked on the basis of tdTomato signal and morphological exclusion of dead cells (fig. S3A). U118-Luc tumor cells cocultured with control CD19.28.BB.ζ CAR-T cells grew similarly to tumor cells alone, whereas both the B7-H3.TMI.ζ and B7-H3.28.BB.ζ CAR-T cells cleared the tumor cells (Fig. 2E and fig. S3B). This finding was recapitulated in HCC827-Luc cocultures (Fig. 2F and fig. S3C).

Last, we evaluated the cytokine release profile of B7-H3.TMI.ζ and B7-H3.28.BB.ζ CAR-T cells using a multiplexed flow cytometry bead assay measuring the following cytokines: interleukin(IL)-2, IL-4, IL-5, IL-6, IL-9, IL-10, IL-13, IL-17A, IL-17F, IL-22, interferon-γ (IFN-γ), and tumor necrosis factor–α (TNF-α). After coculture with HCC827 tumor cells, both B7-H3.TMI.ζ and B7-H3.28.BB.ζ CAR-T cells released more cytokines across all cytokines tested compared

to control CD19.28.BB.ζ CAR-T cells (Fig. 2G). Intriguingly, we found that B7-H3.TMI.ζ CAR-T cells released significantly lower concentrations of these cytokines than B7-H3.28.BB.ζ CAR-T cells apart from IL-6.

Together, these results demonstrated that B7-H3.TMI.ζ and B7-H3.28.BB.ζ CAR-T cells showed equivalent cytotoxic responses and killing kinetics in vitro. While the cytokine secretion profile of these CAR-T cells was similar, B7-H3.TMI.ζ CAR-T cells mostly secreted lower amounts of these cytokines compared to B7-H3.28.BB.ζ CAR-T cells.

Antitumor responses of B7-H3.TMI.ζ and B7-H3.28.BB.ζ CAR-T cells in vivo

We next assessed the in vivo antitumor responses of our lead B7-H3 CARs in three orthotopic solid tumor models. All human tumor cell lines (HCC827, U118, and PANC-1) were stably transfected with a plasmid containing Luciferase and tdTomato (-Luc) to allow for in vivo tracking by bioluminescent imaging. We first tested our CARs in a lung cancer model. HCC827-Luc tumor cells were injected intravenously into NOD.Cg-*Prkdc^{scid} Il2rg^{tm1Wjl}*/SzJ (NSG) mice followed by injection of B7-H3.TMI.ζ, B7-H3.28.BB.ζ, or control CD19.28.BB.ζ CAR-T cells intravenously 3 and 10 days later (Fig. 3A). B7-H3.TMI.ζ and B7-H3.28.BB.ζ CAR-T cells reduced tumor burden and showed a concomitant increase of overall survival compared to CD19.28.BB.ζ CAR-T (Fig. 3, B to D).

We then explored our CAR-T cell therapy in an orthoptic GBM model. We intracranially injected U118-Luc cells into the right cerebral hemisphere of NSG mice followed by an injection of CAR-T cells intratumorally 7 days later (Fig. 3E) as it has been shown that intratumorally injected CAR-T cells confer superior antitumor responses than intravenous injected CAR-T cells at equivalent low doses (28). Both B7-H3.TMI.ζ and B7-H3.28.BB.ζ CAR-T cells evoked potent antitumor responses compared to CD19.28.BB.ζ CAR-T cells (Fig. 3, F and G). There was no difference in tumor burden between the B7-H3.TMI.ζ and B7-H3.28.BB.ζ CAR-T cells (Fig. 3, F and G). Intriguingly, we found that, while both B7-H3 CAR-T cells improved overall survival compared to CD19 CAR-T cells, B7-H3.TMI.ζ CAR-T cells had superior survival outcomes compared to B7-H3.28.BB.ζ CAR-T cells (Fig. 3H). We did not see substantial tumor burden before death in B7-H3.28.BB.ζ CAR-T cell–treated mice, suggesting that the CAR-T cells and not the tumor were the cause of death in this cohort of mice (fig. S4A).

Last, we examined our CAR-T cell therapy in an orthotopic model of pancreatic cancer. We orthotopically injected NSG mice with PANC-1-Luc tumor cells into the pancreas, followed by intravenous injections of CAR-T cells 7 and 14 days later (Fig. 3I). Both B7-H3 CAR-T cells reduced tumor burden and improved overall survival compared to control CD19.28.BB.ζ CAR-T cells (Fig. 3, J to L, and fig. S4B). We noted a trend that B7-H3.TMI.ζ CAR-T cells better reduced tumor burden compared to B7-H3.28.BB.ζ CAR-T cells, although this only reached statistical significance on day 21 (Fig. 3K). Similarly, there was a trend toward improved survival in B7-H3.TMI.ζ CAR-T cells compared to B7-H3.28.BB.ζ CAR-T cells, with four of the seven B7-H3.TMI.ζ CAR-T cell–treated alive 100 days after tumor cell injection compared to one of the seven B7-H3.28.BB.ζ CAR-T cell–treated mice (Fig. 3L).

Together, these experiments demonstrated that B7-H3.TMI.ζ and B7-H3.28.BB.ζ CAR-T cells exhibited antitumor responses against multiple tumor models in vivo. Further, B7-H3.TMI.ζ CAR-T cells
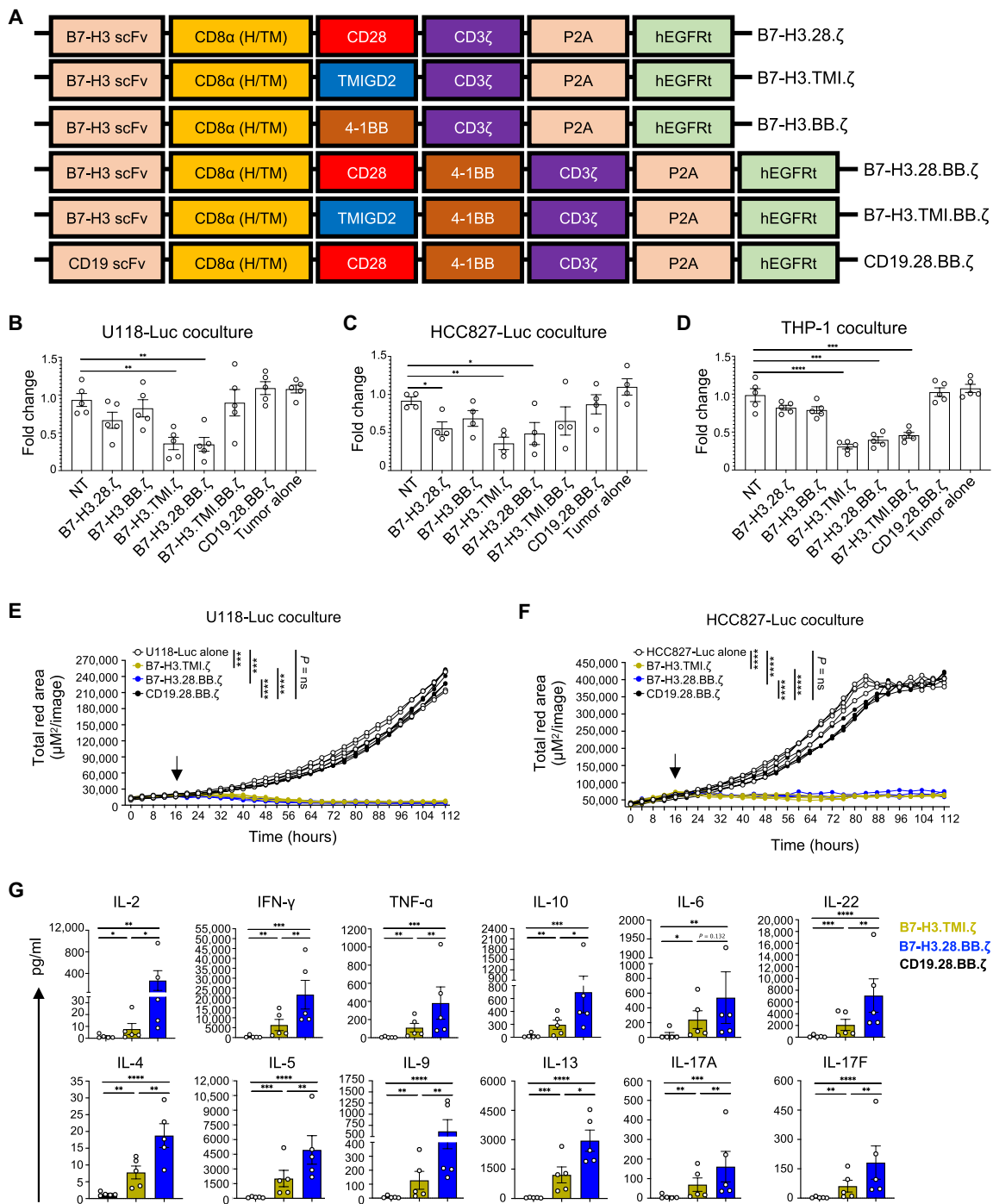
Fig. 2. B7-H3.TMI.ζ CAR-T cells demonstrate antitumor responses in vitro. (**A**) Schematic depicting B7-H3 and CD19 CAR construct designs. (**B**) Single-killing coculture assay of CAR-T cells and U118-Luc tumor cells. Transduction efficiency of CAR-T cells was adjusted to 50%. $n = 5$. Effector:target (E:T) ratio of 10:1. (**C**) Single-killing coculture assay of CAR-T cells and HCC827-Luc tumor cells. Transduction efficiency of CAR-T cells was adjusted to 50%. $n = 4$. E:T ratio of 10:1. (**D**) Single-killing coculture assay of CAR-T cells and THP-1 tumor cells. Transduction efficiency of CAR-T cells was adjusted to 50%. $n = 5$. E:T ratio of 1:1. (**E**) Tumor growth curve from time-lapse coculture assay of CAR-T cells and U118-Luc tumor cells. Black arrow indicates the addition of CAR-T cells. Tumor burden was quantified on the basis of the area of red signal (tdTomato) over time. $n = 4$. E:T ratio of 20:1. (**F**). Tumor growth curve from time-lapse coculture assay of CAR-T cells and HCC827-Luc tumor cells. Black arrow indicates the addition of CAR-T cells. Tumor burden was quantified on the basis of the area of red signal (tdTomato) over time. $n = 4$. E:T ratio of 20:1. ns, not significant. (**G**) CAR-T cell cytokine release after 24-hour coculture with HCC827 tumor cells in vitro. $n = 5$. E:T ratio of 4:1. Data points in (B) to (D) and (G) are the average of duplicate values for four or five unique donors. Data points in (E) and (F) are the average of triplicate wells for four unique donors. Bars graphs denote means ± SEM. *$P < 0.05$, **$P < 0.01$, ***$P < 0.001$, and ****$P < 0.0001$ via unpaired t test on regular [(B) to (D)] or log-transformed (G) data or via two-way analysis of variance (ANOVA) with Tukey's multiple comparisons test at the final imaging time point [(E) and (F)].
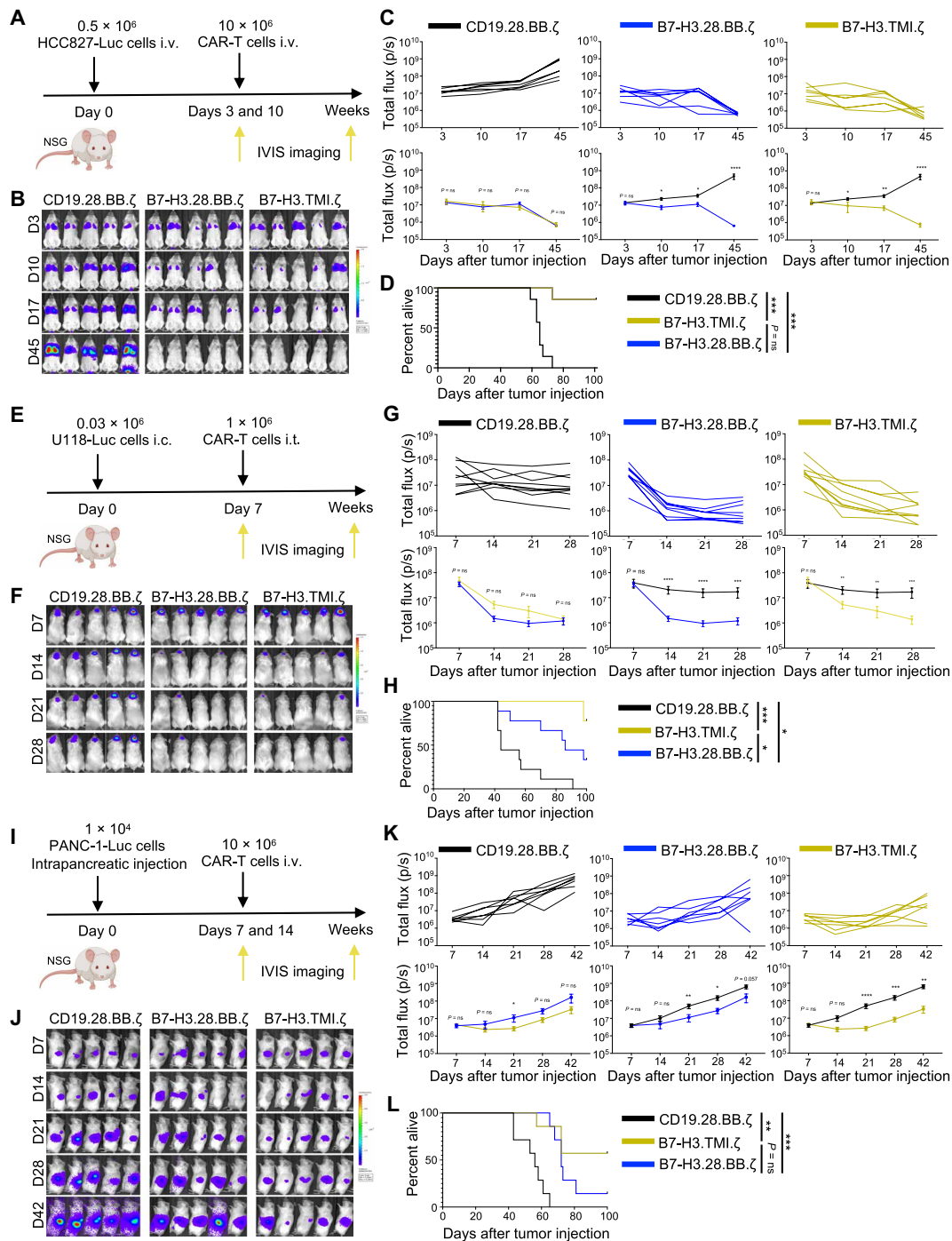
Fig. 3. B7-H3.TMI.ζ CAR-T cells show equivalent or superior antitumor responses compared to B7-H3.28.BB.ζ CAR-T cells in vivo. (**A** to **D**) HCC827-Luc metastasis lung cancer model. $n = 7$ mice per group. (A) Experimental design timeline. (B) Representative bioluminescent images covering time points when all mice remained alive. (C) Quantification of tumor signal shown from individual mice (top row) and summary data comparing each CAR-T cell grouping during time points when all mice remained alive. (D) Kaplan-Meier survival curve of CAR-T cell groups. (**E** to **H**) U118-Luc orthotopic GBM cancer model. $n = 9$ mice per group. (E) Experimental design timeline. (F) Representative bioluminescent images covering time points when all mice remained alive. (G) Quantification of tumor signal shown from individual mice (top row) and summary data comparing each CAR-T cell grouping during time points when all mice remained alive. (H) Kaplan-Meier survival curve of CAR-T cell groups. (**I** to **L**) PANC-1-Luc orthotopic pancreatic cancer model. $n = 7$ mice per group. (I) Experimental design timeline. (J) Representative bioluminescent images covering time points when all mice remained alive. (K) Quantification of tumor signal shown from individual mice (top row) and summary data comparing each CAR-T cell grouping during time points when all mice remained alive. (L) Kaplan-Meier survival curve of CAR-T cell groups. Two unique T cell donors were used in each tumor model. Line graphs in the bottom row of (C), (G), and (K) denote means ± SEM. *$P < 0.05$, **$P < 0.01$, ***$P < 0.001$, and ****$P < 0.0001$ via one-way ANOVA with Tukey's multiple comparisons test of log-transformed data at each time point [(C), (G), and (K)] or log-rank test [(D), (H), and (L)]. i.v., intravenous; i.c., intracranial; i.t., intratumoral.

demonstrated equivalent or superior outcomes in a tumor-dependent manner.

Persistence of B7-H3.TMI.ζ and B7-H3.28.BB.ζ CAR-T cells in vivo

Having established that our B7-H3 CAR-T cells were cytolytic in multiple tumor models in vivo, we next examined the expansion and persistence of these B7-H3 CAR-T cells in vivo. We modified our original CAR constructs to include a self-cleaving T2A peptide followed by a luciferase (CAR-Luc) to allow for in vivo CAR-T cell tracking using bioluminescent imaging (Fig. 4A). We injected NSG mice with parental HCC827 cells that do not express a luciferase, followed by a single, subtherapeutic injection of B7-H3.TMI.ζ-Luc, B7-H3.28.BB.ζ-Luc, or CD19.28.BB.ζ-Luc CAR-T cells intravenously (Fig. 4B). On day 7, CAR-Luc signal was detectable in all constructs, and there was no difference between any group; beginning on day 21, both B7-H3 CAR-Luc T cells had significantly higher signal than CD19 CAR-Luc T cells; however, by day 46, B7-H3.TMI.ζ-Luc but not B7-H3.28.BB.ζ-Luc CAR-T cells showed significantly higher CAR-Luc signal than CD19.28.BB.ζ-Luc CAR-T cells, suggesting that B7-H3.TMI.ζ-Luc CAR-T cells can persist longer that B7-H3.28.BB.ζ-Luc CAR-T cells in vivo, although the latter did approach statistical significance (Fig. 4, C to E).

Examination of the peak CAR-Luc signal from each mouse throughout the experiment revealed that B7-H3.TMI.ζ-Luc and B7-H3.28.BBζ-Luc CAR-T cells expanded to a similar degree that was higher than CD19.28.BB.ζ-Luc CAR-T cells (Fig. 4F). Examining the number of T cells in the lungs, spleen, and blood of CAR-Luc–treated mice at the end of the experiment demonstrated that B7-H3 CAR-Luc T cells were present in greater numbers than CD19.28.BB.ζ-Luc CAR-T cells and at equivalent numbers between the B7-H3 CAR-Luc T cell constructs (Fig. 4, G to I). Together, these data suggested that both B7-H3 CAR Luc-T cells could expand and persist in vivo in an antigen-dependent manner. Further, B7-H3.TMI.ζ-Luc CAR-T cells had modestly improved persistence compared to B7-H3.28.BB.ζ-Luc CAR-T at late time points.

Transcriptomic differences between B7-H3.TMI.ζ and B7-H3.28.BB.ζ CAR-T cells in vitro

To gain mechanistic insight into our CAR-T cell therapy, we performed RNA sequencing comparing B7-H3.TMI.ζ and B7-H3.28.BB.ζ CAR-T cells to CD19.28.BB.ζ CAR-T cells after coculture with HCC827 tumor cells for 24 hours in vitro. Compared to CD19.28.BB.ζ CAR-T cells, both B7-H3.TMI.ζ and B7-H3.28.BB.ζ CAR-T cells showed broad transcriptomic differences (Fig. 5A). We found 307 shared differentially expressed genes (DEGs), and 198 and 153 unique DEGs between the B7-H3.TMI.ζ and B7-H3.28.BB.ζ CAR-T cells, respectively (Fig. 5B and tables S1 and S2). Gene set enrichment analysis (GSEA) revealed many enriched pathways in both B7-H3 CAR-T cells compared to CD19 CAR-T cells, with a high degree of similarity in terms of the pathways expressed but variability in the order of their enrichment (Fig. 5C and tables S3 and S4). Among the top enriched pathways, we found the "oxidative phosphorylation" pathway in B7-H3.TMI.ζ CAR-T cells compared to the "glycolysis" pathway in the B7-H3.28.BB.ζ CAR-T cells (Fig. 5C), suggesting metabolic differences between these two CAR-T cells.

To further validate these findings, we used Seahorse T cell metabolic profiling to measure changes in the % adenosine 5′-triphosphate (%ATP) generated from glycolysis and mitochondria after coculture and at baseline (cultured in the absence of tumor cells). In these assays, the %ATP generated from glycolysis and the %ATP generated from mitochondria sum to 100%; thus, these values are dependent on one another. Upon acute 24-hour stimulation, B7-H3.TMI.ζ CAR-T cells had a lower %ATP generated from glycolysis (Fig. 5D, left graph) and a concomitant higher %ATP from mitochondria (Fig. 5D, right graph) at baseline and after coculture compared to B7-H3.28.BB.ζ CAR-T cells. After chronic stimulation with repeated tumor cell additions, B7-H3.TMI.ζ CAR-T cells did not exhibit differences in the %ATP generated from glycolysis or mitochondria at baseline but did generate a lower %ATP from glycolysis and concomitant higher %ATP from mitochondria after coculture (Fig. 5E). In both conditions, we observed that B7-H3.TMI.ζ CAR-T cells maintained their metabolic signature, while B7-H3.28.BB.ζ CAR-T cells modestly increased their glycolytic energy expenditure with an accompanying decrease in mitochondrial energy expenditure (Fig. 5, D and E). Thus, these functional metabolic results recapitulated our RNA sequencing experimental findings.

As the %ATP from glycolysis or mitochondria is a relative comparison of total ATP generation, we next explored whether absolute changes in the extracellular acidification rate (ECAR), oxygen consumption rate (OCR), and spare respiratory capacity were present. Coculture with HCC827 tumor cells led to a lower ECAR (fig. S5A) and equivalent OCR (fig. S5B) in B7-H3.TMI.ζ CAR-T cells compared to B7-H3.28.BB.ζ CAR-T cells. The OCR/ECAR ratio was higher in B7-H3.TMI.ζ CAR-T cells than B7-H3.28.BB.ζ CAR-T cells (fig. S5C), consistent with our findings of a larger relative contribution of mitochondrial metabolism in B7-H3.TMI.ζ CAR-T cells compared to B7-H3.28.BB.ζ CAR-T cells. Last, there was no difference in the spare respiratory capacity between the two CAR constructs (fig. S5D).

We also sought to determine what mitochondrial metabolic pathways were key to B7-H3.TMI.ζ CAR-T cell mitochondrial metabolism using Seahorse substrate oxidation stress testing. After coculture with HCC827 tumor cells and Seahorse analysis in the presence of pathway-specific inhibitors (e.g., Etomoxir for long-chain fatty acids, bis-2-(5-phenylacetamido-1,3,4-thiadiazol-2-yl)-ethyl sulfide (BPTES) for glutamine, or UK5099 for glucose/pyruvate), B7-H3.TMI.ζ CAR-T cells reached a lower maximal OCR than B7-H3.28.BB.ζ CAR-T cells under long-chain fatty acid oxidation inhibition (fig. S5E), indicating a greater reliance on this metabolic pathway. There was also a trend toward a lower maximal OCR in B7-H3.TMI.ζ CAR-T cells under glutamine oxidation inhibition as well (fig. S5F), but this was not statistically significant ($P = 0.15$). Last, there was no difference between the two B7-H3 CAR-T cell constructs under glucose/pyruvate oxidation inhibition (fig. S5G).

To directly compare B7-H3.TMI.ζ and B7-H3.28.BB.ζ CAR-T cells, we performed an additional RNA sequencing experiment from RNA isolated after 72 hours of coculture with HCC827 tumor cells. Broad transcriptomic differences between these two B7-H3 CARs were present, with a total of 1328 DEGs identified (Fig. 5F and table S5). GSEA revealed four metabolic pathways negatively enriched in B7-H3.TMI.ζ CAR-T cells, including "oxidative phosphorylation," "fatty acid metabolism," "adipogenesis," and "glycolysis" (Fig. 5G and table S6). These results suggest that B7-H3.TMI.ζ CAR-T cells were overall less metabolically active than B7-H3.28.BB.ζ CAR-T cells after 72 hours of coculture. To determine which pathway(s) contributed the largest role, we performed overrepresentation analysis (ORA) by examining what pathways were overrepresented among the most
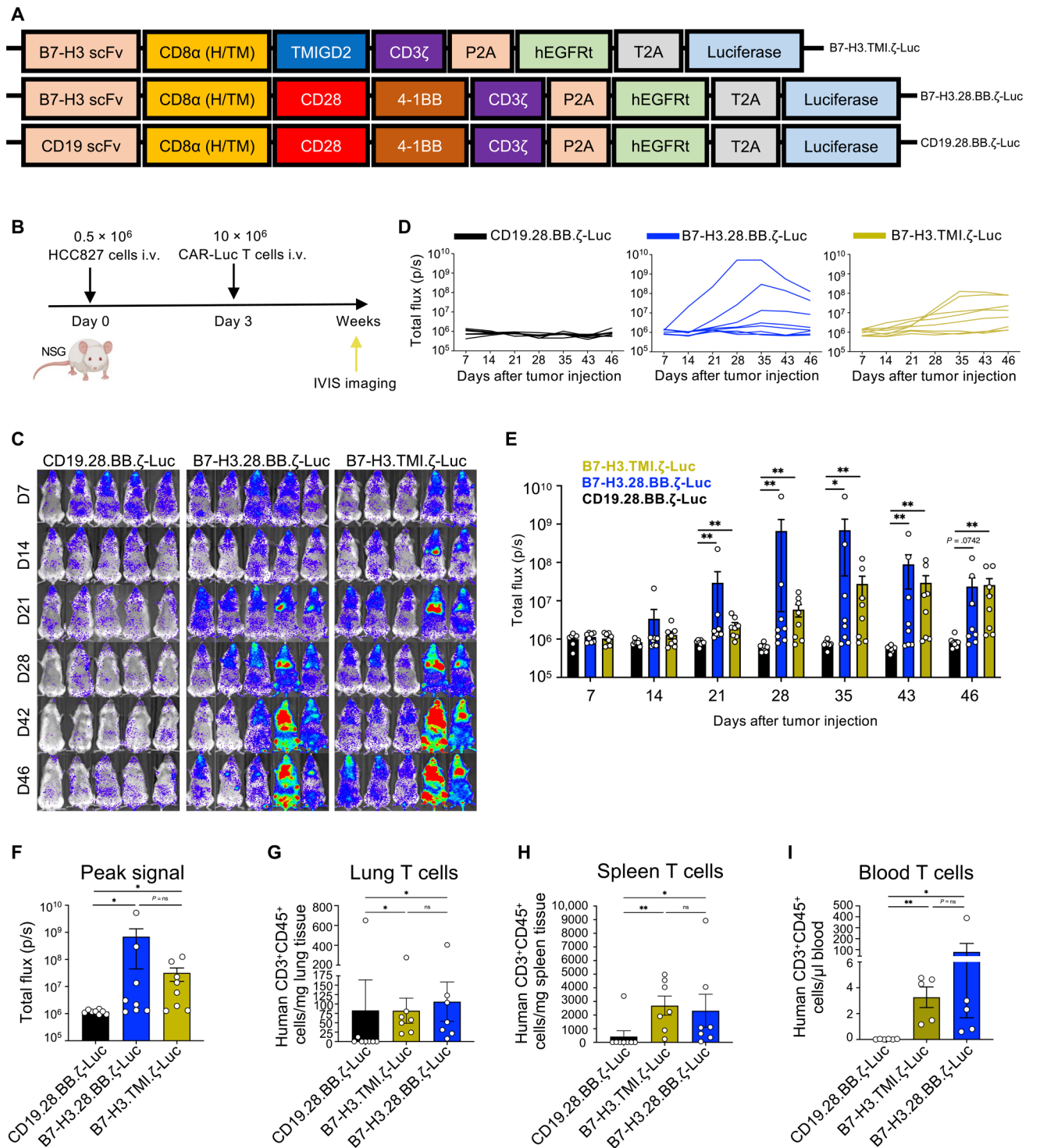
Fig. 4. B7-H3.TMI.ζ CAR-T cells show long-term persistence in vivo. (**A**) CAR-Luc construct schematics. (**B**) Experimental design of the CAR-Luc T cell experiment. (**C**) Representative bioluminescent images. (**D**) Line graphs depicting individual mouse CAR-Luciferase T cell signal throughout the experiment. (**E**) Bar graph comparing CAR-Luc T cell signal at each time point. (**F**) Peak bioluminescent signal from each mouse over the course of the experiment. (**G** to **I**) Quantification of T cells in lung tissue (G), spleen tissue (H), and blood (I). $n = 7$ to 8 mice per group from two unique T cell donors in (B) to (H). $n = 5$ mice from one unique T cell donor in (I). Bar graphs denote means ± SEM. $*P < 0.05$ and $**P < 0.01$ via the Kruskal Wallis test [(D) to (I)].
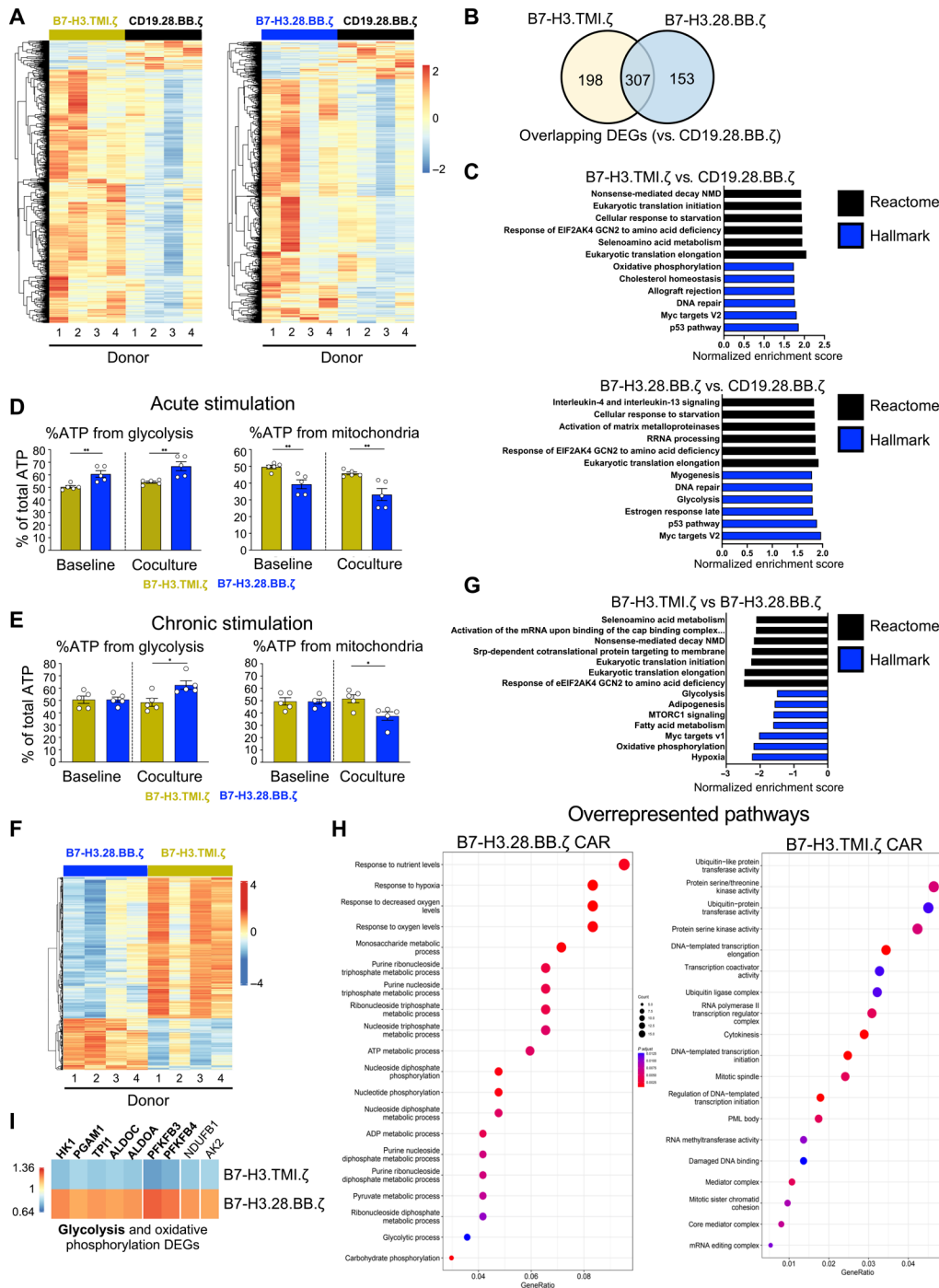
Fig. 5. B7-H3.TMI.ζ CAR-T cells maintain metabolic pathways, whereas B7-H3.28.BB.ζ CAR-T cells increase glycolytic pathways in vitro. (**A** to **C**) RNA sequencing data comparing B7-H3.TMI.ζ CAR-T cells or B7-H3.28.BB.ζ CAR-T cells to CD19.TMI.ζ CAR-T cells after in vitro coculture with HCC827 tumor cells for 24 hours. $n = 4$. (A) Heatmap depicting all DEGs (P adj. < 0.05; absolute $\log_2$ fold change > 0.5) from B7-H3.TMI.ζ CAR-T cells (left) and B7-H3.28.BB.ζ CAR-T cells versus CD19.28.BB.ζ CAR-T cells. (B) Venn diagram showing unique and shared DEGs between B7-H3.TMI.ζ CAR-T cells and B7-H3.28.BB.ζ CAR-T cells. (C) Gene set enrichment analysis (GSEA) pathway analysis comparing B7-H3.TMI.ζ (top) and B7-H3.28.BB.ζ CAR-T cells (bottom) versus CD19.28.BB.ζ CAR-T cells. Pathways were obtained from Reactome (black) and Hallmark (blue) datasets. (**D**) Comparison of %ATP generated from glycolysis (left) and mitochondria (right) in B7-H3.TMI.ζ versus B7-H3.28.BB.ζ CAR-T cells cultured without tumor cells (baseline) or with HCC827 tumor cells (coculture) for 24 hours. (**E**) Graphs depicted as in (D) but after 7 days with repeated additions of tumor cells. (**F** to **I**) RNA sequencing analysis comparing B7-H3.TMI.ζ and B7-H3.28.BB.ζ CAR-T cell after 72 hours of coculture with HCC827 tumor cells. $n = 4$. (F) Heatmap depicting DEGs from B7-H3.TMI.ζ CAR-T cells compared to B7-H3.28.BB.ζ CAR-T cells. (G) GSEA pathway analysis of RNA sequencing data. Reactome pathways are shown in black, and Hallmark pathways are shown in blue. (H) Dot plot depicting overrepresentation analysis (ORA) of highly expressed DEGs (absolute fold change > 1.5). (I) Heatmap of DEGs from curated gene set describing glycolysis and oxidative phosphorylation proteins. Graphs in (D) and (E) denote means ± SEM. *P < 0.05 and **P < 0.01 via Student's t test.

highly expressed DEGs (P adj. < 0.05; absolute fold change > 1.5). ORA revealed "glycolytic process" as the only overrepresented metabolic pathway in B7-H3.28.BB.ζ CAR-T cells from the list above, with other pathways broadly describing hypoxia or nucleotide processes. (Fig. 5H). B7-H3.TMI.ζ CAR-T cells broadly showed pathways associated with transcription, mitosis, and ubiquitination (Fig. 5H).

Using a previously published gene set (table S7) describing key enzymes, regulatory proteins, accessory proteins, and other related genes in glycolysis and oxidative phosphorylation (29), we found seven down-regulated DEGs associated with classical glycolysis enzymes or regulation of glycolysis (HK1, PGAM1, TPI1, ALDOC, ALDOA, PFKFB3, and PFKFB4) and two down-regulated DEGs associated with a subunit or other function in oxidative phosphorylation (NFDFB1 and AK2) in B7-H3.TMI.ζ CAR-T cells compared to B7-H3.28.BB.ζ CAR-T cells in our RNA sequencing dataset (Fig. 5I). To validate our findings at the protein level, we cocultured B7-H3 CAR-T cells with HCC827 tumor cells and used a previously described flow cytometry metabolic gene staining approach (30) to directly detect four glycolysis-associated proteins found in our experiments: aldolase A (ALDOA), 6-phosphofructo-2-kinase/fructose-2,6-biphosphatase 3 (PFKFB3), hexokinase 1 (HK1), and solute carrier family 16 member 3 (SLC16A3). B7-H3.TMI.ζ CAR-T cells had a lower ALDOA, PFKFB3, and HK1 median fluorescent intensity (MFI) compared to B7-H3.28.BB.ζ CAR-T cells (fig. S6, A to C). In addition, SLC16A3 (MCT4), which has been shown at the mRNA level to trend toward higher expression in CAR-T cells with a CD28 costimulatory domain compared to a 4-1BB costimulatory domain (13), also had a lower MFI in B7-H3.TMI.ζ CAR-T cells (fig. S6D). Together, these data suggested that B7-H3.TMI.ζ CAR-T cells were not as reliant on glycolytic pathways as B7-H3.28.BB.ζ CAR-T cells.

Distinct in vivo transcriptional programs between B7-H3.TMI.ζ and B7-H3.28.BB.ζ CAR-T cells

The tumor microenvironment plays a major role in modulating CAR-T cell function and phenotype which can have profound impacts on therapeutic responses (31). We therefore examined how the tumor microenvironment would affect transcriptional programs in our B7-H3 CAR-T cells. We performed RNA sequencing from lung-infiltrating T cells collected from the lungs of lung tumor–bearing mice 7 days after B7-H3 CAR-T cell injection. We found broad transcriptomic differences and 945 DEGs between our B7-H3 CAR-T cells (Fig. 6A and table S8). Examining the top enriched pathways by GSEA revealed that B7-H3.TMI.ζ CAR-T cells were positively enriched for pathways broadly describing RNA- and DNA-associated processes (Fig. 6B and table S9). ORA revealed that B7-H3.28.BB.ζ CAR T cells had overrepresented pathways broadly encompassing cytokines and chemokine pathways among others, and, while B7-H3.TMI.ζ CAR-T cells did not show statistically significant overrepresented pathways (P adj. < 0.05) due to few genes meeting the log₂ fold change cutoff, overrepresented pathways approaching significance (P adj. < 0.1) described lysosomal and vacuole pathways (Fig. 6C). Using the same metabolism gene set as before (table S7) (29), we analyzed metabolism-associated gene signatures in this dataset. We found six DEGs associated with glycolysis enzymes and regulatory proteins down-regulated in B7-H3.TMI.ζ CAR-T cells (PFKM, GAPDH, PFKFB3, PFKFB2, HIF1A, and PFKFB4) and no genes associated with oxidative phosphorylation compared to B7-H3.28.BB.ζ CAR-T cells (Fig. 6D).

Using a recently described T cell dysfunction gene signature (table S7) (32), we found 12 DEGs were down-regulated (IL2RA, PLS3, DUSP4, GZMB, PHLDA1, CSF1, TNFRSF18, NDFIP2, AHI1, CDK6, LAYN, and HAVCR2) compared to only one up-regulated gene (KLRC1) in B7-H3.TMI.ζ CAR-T cells compared to B7-H3.28.BB.ζ CAR-T cells in this RNA sequencing dataset (Fig. 6E). Examining a hand-curated gene list of immune inhibitory receptors and ligands (table S7), we found that B7-H3.TMI.ζ CAR-T cells showed six down-regulated DEGs (BTLA, HAVCR2, PDCD1, CTLA4, PDCDLG2, and CD274), compared to B7-H3.28.BB.ζ CAR T cells also in this dataset (Fig. 6F). Together, these data suggested that B7-H3.TMI.ζ and B7-H3.28.BB.ζ CAR-T cells function differently within the in vivo tumor microenvironment, with the former showing a less glycolytic, less dysfunctional, and less immunoinhibitory phenotype compared to the latter.

Last, we analyzed common significant genes (P adj. < 0.05) between our in vivo and in vitro RNA sequencing experiments that directly compared the two B7-H3 CAR-T cells. We hypothesized that genes overexpressed in both experiments would be among the most important for each B7-H3 CAR given that they appear in multiple contexts. We found 85 genes in the B7-H3.TMI.ζ CAR and 67 shared genes in B7-H3.28.BB.ζ CAR (Fig. 6G). ORA of these common genes revealed numerous overrepresented pathways in both CAR constructs (Fig. 6H). In the B7-H3.TMI.ζ CAR, pathways broadly related to endosomes, lysosomes, autophagy, and others were present. In the B7-H3.28.BB.ζ CAR, pathways broadly related to hypoxia and nucleotide metabolism were present among others; notably, glycolytic process also appeared in this list. Together, these results revealed that, when examining common DEGs across experiments, B7-H3.TMI.ζ and B7-H3.28.BB.ζ CAR-T cells had distinct pathway signatures.

Different phenotypic changes between B7-H3.TMI.ζ and B7-H3.28.BB.ζ CAR-T cells after chronic antigen exposure

Persistent exposure to antigens can lead to dysfunctional phenotypes and suboptimal effector responses in CAR-T cells (32). In this setting, different CAR constructions can greatly influence the expression of a variety of cell surface markers (33, 34). To examine whether our TMIGD2 and CD28.4-1BB costimulatory domains would also differentially alter cell surface protein expression, we adapted an in vitro model of chronic antigen exposure (CAE) wherein CAR-T cells were continuously cultured with sufficient HCC827 tumor cells so that the tumor cells were always present in the coculture (32). We directly compared the phenotype of CD3$^+$, CD4$^+$, and CD8$^+$ CAR$^+$ B7-H3.TMI.ζ and B7-H3.28.BB.ζ CAR-T cells at each analysis time point over the course of 17 days of coculture with HCC827 tumor cells (gating strategy shown in fig. S7). Describing first the results from the total CD3$^+$ CAR$^+$ population, we observed global changes between our two B7-H3 CAR populations via t-distributed stochastic neighbor embedding (t-SNE) analysis generated from CAR$^+$ cells at all time points (Fig. 7A). CAR expression decreased in both B7-H3 CAR-T cells, with B7-H3. TMI.ζ CAR-T cells showing fewer CAR$^+$ cells on day 17 (Fig. 7B), a finding consistent with the observation of decreased surface CAR expression post-tumor encounter by other groups who reported an 80% reduction (35) or a reduction from a baseline of 30 to 50% transduction efficiency to less than half (or even approaching zero) in most donors by visual inspection of published graphs (32). Looking at PD-1$^+$ TIM-3$^+$ LAG-3$^+$ exhausted CAR-T cells, we found that
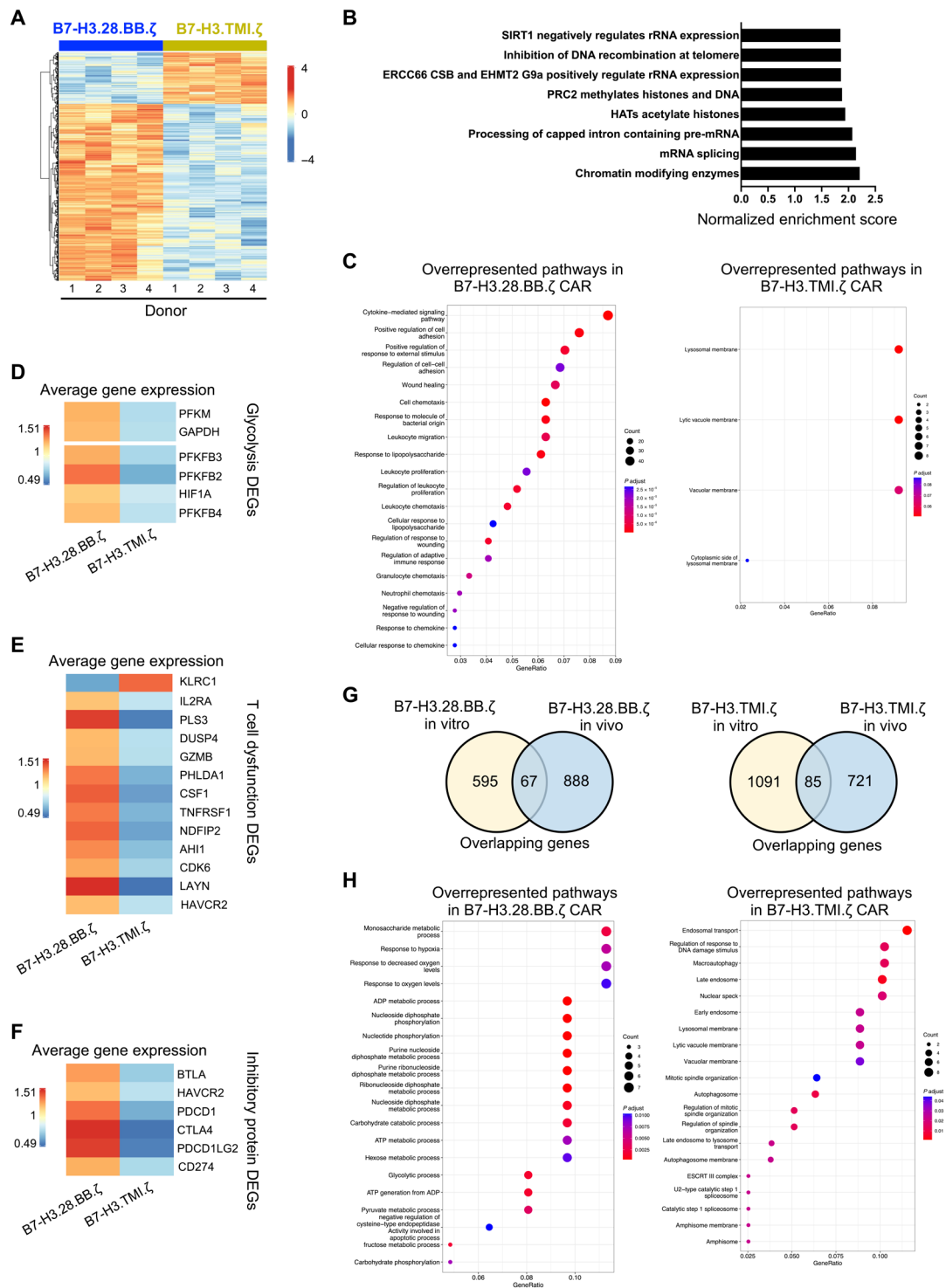
Fig. 6. Tumor-infiltrating B7-H3.TMI.ζ CAR-T cells show a less glycolytic, less dysfunctional, and less inhibited transcriptional signature in lung tumor-bearing mice. (**A** to **F**) RNA sequencing analysis of in vivo lung-infiltrating T cells. *n* = 4. (A) Heatmap depicting DEGs from in vivo lung-infiltrating T cells in mice injected with B7-H3.TMI.ζ CAR-T cells compared to B7-H3.28.BB.ζ CAR-T cells. (B) GSEA pathway analysis of DEGs. (C) ORA of highly expressed DEGs (absolute fold change > 1.5). (D) Heat-map depicting average gene expression of DEGs found in the metabolism gene signature. (E) Heatmap depicting average gene expression of DEGs found in T cell dysfunction gene signature. (F) Heatmap depicting average gene expression of DEGs found in inhibitory protein gene signature. (**G**) Venn diagram showing overlapping significant genes (*P* adj. < 0.05) in either B7-H3.TMI.ζ or B7-H3.28.BB.ζ CAR-T cells from in vivo and in vitro RNA sequencing experiments directly comparing the two con-structs. (**H**) ORA of shared genes in (G). ADP, adenosine 5′-diphosphate.
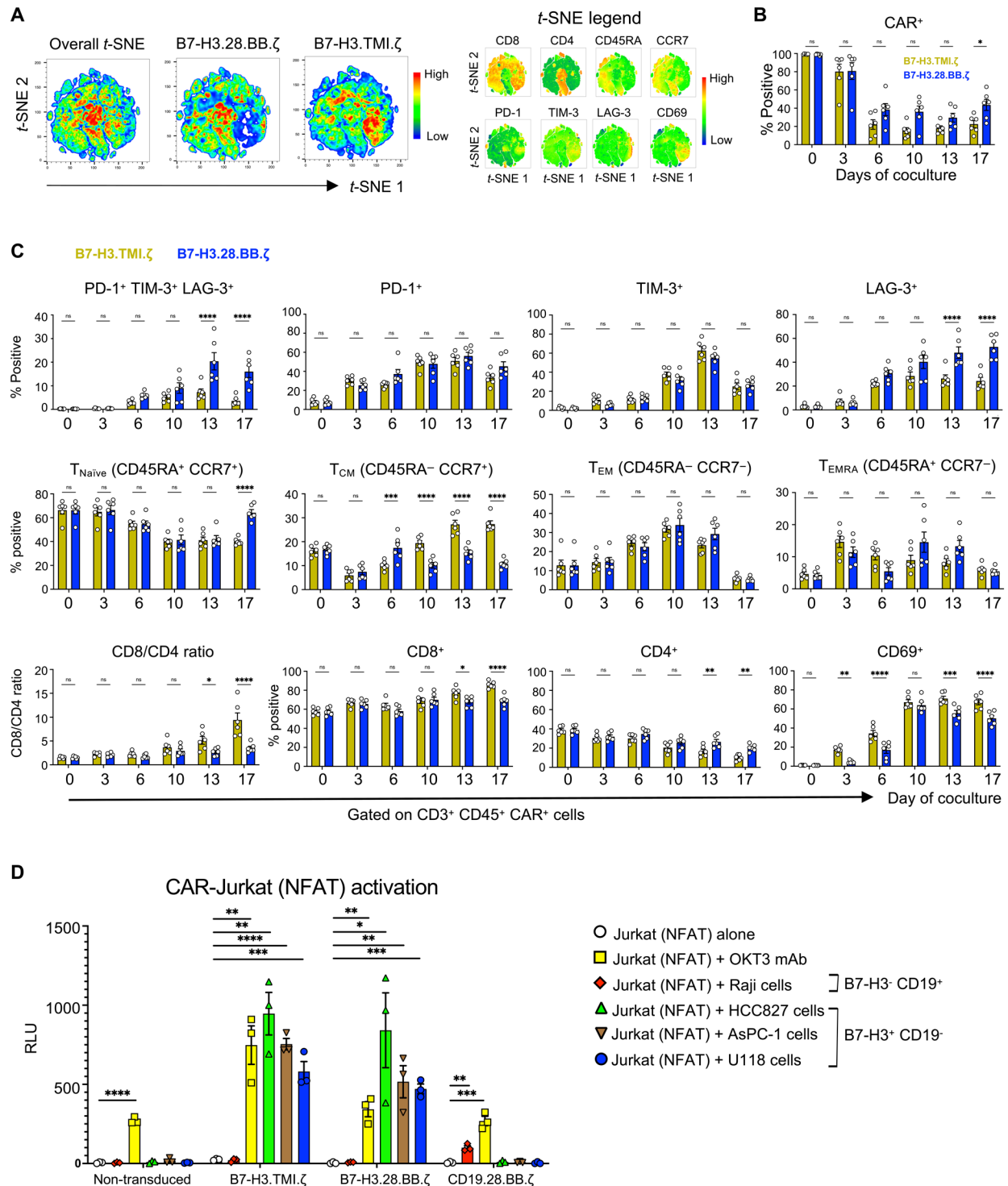
Fig. 7. B7-H3.TMI.ζ CAR-T cells show alterations in exhaustion, memory, and CD8/CD4 ratios after chronic antigen exposure. (**A** to **C**) Phenotypic analysis comparing B7-H3.TMI.ζ and B7-H3.28.BB.ζ CAR-T cells after CAE with HCC827 tumor cells. $n = 6$. (A) t-SNE plots from CAR$^+$ populations. (B) CAR transduction efficiency during CAE. (C) Graphs depicting cell surface markers used to phenotype exhaustion, memory, activation, and CD8/CD4 CAR-T cell populations during CAE. (**D**) Luciferase signal from non-transduced, B7-H3.TMI.ζ, B7-H3.28.BB.ζ, or CD19-28.BB.ζ CAR-transduced Jurkat (NFAT) cells after culture in the indicated conditions. $n = 3$. Data points in (B) to (D) are the average of triplicate values. Data in represent three independent experiments (D) and or six different donors [(A) to (C)]. Bar graphs show means ± SEM. $*P < 0.05$, $**P < 0.01$, $***P < 0.001$, and $****P < 0.0001$ via two-way ANOVA with Šídák's multiple comparisons test [(B) and (C)] or Student's t test comparing values only to Jurkat (NFAT) cells alone (D). RLU, relative light units; T$_{Naïve}$, naïve T cells; T$_{CM}$, central memory T cells; T$_{EM}$, effector memory T cells; T$_{EMRA}$, terminally differentiated effector memory T cells.

B7-H3.TMI.ζ CAR-T cells acquired fewer exhausted cells by days 13 and 17 than B7-H3.28.BB.ζ CAR-T cells (Fig. 7C). As differences in the expression of programmed cell death protein 1 (PD-1), T cell immunoglobulin and mucin domain-containing protein 3 (TIM-3), lymphocyte-activation gene 3 (LAG-3), or a combination could underlie this finding, we subsequently examined each protein individually. We did not detect differences in PD-1 or TIM-3 expression (Fig. 7C). By contrast, we found that LAG-3 expression in B7-H3. TMI.ζ CAR T cells was significantly lower on days 13 and 17 compared to B7-H3.28.BB.ζ CAR T cells (Fig. 7C).

We examined whether changes in exhaustion phenotype were present in vivo as well by isolating intratumorally injected CAR-T cells from subcutaneously implanted HCC827 tumors in NSG mice. Similar to our in vitro findings, LAG-3 expression was lower in B7-H3.TMI.ζ CAR-T cells compared to B7-H3.28.BB.ζ CAR-T cells, and there was no difference in either PD-1 or TIM-3 expression (fig. S8A). By contrast, PD-1$^+$ TIM-3$^+$ LAG-3$^+$ exhausted CAR-T cells were nearly undetectable, likely due to the lower expression of PD-1 and TIM-3 at the analyzed time point (fig. S8A).

When examining memory phenotypes, we found a significantly enriched population of central memory cells (CD45RA$^-$ CCR7$^+$) cells in B7-H3.TMI.ζ CAR-T cells beginning on day 10 onward, while, on day 6, the opposite was true (Fig. 7C). We observed a lower percentage of naïve T cells (CD45RA$^+$ CCR7$^+$) in B7-H3. TMI.ζ CAR-T cells on day 17 and no differences in effector memory (CD45RA$^-$ CCR7$^-$) or terminally differentiated EMRA cells (CD45RA$^+$ CCR7$^-$) between the groups (Fig. 7C). We also found that B7-H3.TMI.ζ CAR-T cells exhibited higher CD69$^+$ expression on days 3 and 6, equivalent expression on day 10, and higher expression on days 13 and 17 compared to B7-H3.28.BB.ζ CAR-T cells (Fig. 7C).

We also examined whether the changes in memory phenotype would be present in vivo as well. Analysis of the in vivo–isolated CAR-T cells described above revealed that the majority of CAR-T cells were of the effector memory or EMRA subsets, with naïve and central memory subsets generally comprising less than 10 to 15% of the total population (fig. S8B), a finding similar to other studies showing that in vivo–isolated CAR-T cells were largely effector memory (CD45RO$^+$ CCR7$^-$) (36) or effector (CD45RO$^-$ CD62L$^-$) and effector memory (CD45RO$^+$ CCD62L$^-$) cells (37). Nevertheless, the percentage of central memory cells was nominally higher, and there was a trend toward fewer EMRA cells ($P = 0.09$) in B7-H3. TMI.ζ CAR-T cells compared to B7-H3.28.BB.ζ CAR-T cells, while there were no differences in the naïve or effector memory populations (fig. S8B), altogether suggestive of an overall less differentiated phenotype.

Last, we found that, while both B7-H3 CAR-T cells showed a trend of decreasing CD4$^+$ T cells and increasing CD8$^+$ T cells, B7-H3. TMI.ζ CAR-T cells showed significantly lower CD4$^+$ T cells, significantly higher CD8$^+$ T cells, and a significantly higher CD8/CD4 T cell ratio compared to B7-H3.28.BB.ζ CAR-T cells beginning on day 13 (Fig. 7C). To validate this finding, we reexamined DEGs from our in vivo RNA sequencing data (Fig. 6) given that this experimental design more closely mimics CAE than our other experiments. We found that the *CD4* gene was a significant down-regulated DEG (P adj. < 0.05; absolute log$_2$ fold change > 0.5) and that the *CD8A* gene was significantly up-regulated (P adj. < 0.05; log$_2$ fold change $= 0.4206$) in B7-H3.TMI.ζ CAR T cells; the *CD8B* gene showed a nonsignificant (P adj. $= 0.161$; log$_2$ fold change $= 0.31$)

up-regulation in B7-H3.TMI.ζ CAR-T cells as well (fig. S9A). To confirm this finding at the protein level, we analyzed lung-infiltrating and splenic T cells from lung tumor–bearing mice 46 days after tumor injection. One donor and associated mice were the same as in Fig. 4, while another donor and associated mice were previously untested. B7-H3.TMI.ζ CAR-T cells showed a higher percentage of CD8$^+$ T cells and lower percent of CD4$^+$ T cells compared to B7-H3.28.BB.ζ CAR-T cells in lung-infiltrating T cells (fig. S9B), whereas splenic T cells showed no difference in either population (fig. S9C).

The trends described above were largely replicated in CD4$^+$ CAR$^+$ and CD8$^+$ CAR$^+$ populations with only minor changes in temporal dynamics (fig. S10) except for notable exceptions described below. B7-H3.TMI.ζ CD4$^+$ CAR$^+$ T cells expressed more TIM-3 on day 10 and lower TIM-3 on days 13 and 17 compared to B7-H3.28.BB.ζ CD4$^+$ CAR$^+$ CAR-T cells (fig. S10A). They also had an equivalent percent of CD69$^+$ cells on day 17 due to a decrease in CD69 expression. B7-H3.TMI.ζ CD8$^+$ CAR$^+$ T cells showed a lower percentage of terminally differentiated effector memory T cells on days 10 and 13 compared to B7-H3.28.BB.ζ CAR-T cells (fig. S10B).

It has been reported that the antigen affinity and T cell receptor (TCR) signaling strength can alter T cell memory formation in CD8$^+$ T cells (38) and that TCR signal strength can affect the expression of PD-1 and LAG-3 (39). As our B7-H3 CARs use the same scFv and thus share the same antigen affinity, we sought to examine whether the TMIGD2 and CD28.4-1BB costimulatory domains alter T cell activation strength as a mechanism underlying the phenotypic differences described above. We transduced a T cell activation reporter cell line, Jurkat [nuclear factor of activated T cells (NFAT)] cells, which express firefly luciferase via NFAT response elements, with our B7-H3.TMI.ζ, B7-H3.28.BB.ζ, and CD19.28. BB.ζ CARs. We cultured non-transduced Jurkat (NFAT) cells or CAR-transduced Jurkat (NFAT) cells either alone, with plate-bound activating anti-CD3 OKT3 antibody, with CD19$^+$ B7-H3$^-$ cells (Raji), or with CD19$^-$ B7-H3$^+$ cell lines (HCC827, AsPC-1, and U118) (Fig. 7D). All jurkat (NFAT) cells signaled in response to OKT3 stimulation and did not signal when cultured alone. B7-H3. TMI.ζ– and B7-H3.28.BB.ζ–transduced Jurkat (NFAT) cells signaled in response to HCC827, AsPC-1, and U118 tumor cell lines to broadly similar degrees but not to Raji cells. Notably, the level was nearly identical for the HCC827 cell line used for CAE stimulation and all RNA sequencing experiments. CD19.28.BB.ζ-transduced Jurkat (NFAT) cells signaled in response to Raji cells but not HCC827, AsPC-1, and U118 tumor cell lines. Together, these results demonstrated that B7-H3.TMI.ζ CAR-T cells acquired differences in memory, exhaustion, activation, and CD8/CD4 phenotype upon CAE.

DISCUSSION

There remains a great need to improve CAR design to achieve successful clinical outcomes in CAR-T cell therapy targeting solid tumors. Here, we developed and tested the TOP CAR, a B7-H3 CAR that included a TMIGD2 costimulatory domain. Comparison to other second- and third-generation constructs revealed that second-generation B7-H3.TMI.ζ and third-generation B7-H3.28. BB.ζ CAR-T cells were the top performing CARs in in vitro killing. B7-H3.TMI.ζ CAR-T cells were also efficacious in multiple solid tumor models, showing equivalent or superior outcomes to B7-H3.28.BB.ζ CAR-T cells. Last, B7-H3.TMI.ζ CAR-T cells showed unique transcriptomic, metabolomic, and phenotypic profiles,

indicating that TMIGD2 costimulation offers distinct benefits from CD28.41BB costimulation.

Two major considerations of CAR design surround the optimal choice of target antigen and costimulatory domain. Among CAR-T cells targeting solid tumors, B7-H3 has emerged as a uniquely promising target, with all published results from early clinical trials all using second-generation CARs (40–43). In our experiments using in vitro killing assays with lowered transduction efficiency, we found that B7-H3.TMI.ζ CAR-T cells but not other second-generation CAR-T cells could kill three different tumor cell lines. Thus, TMIGD2 costimulation may be superior to current FDA-approved CD28 and 4-1BB costimulatory domains (44). A few clinical trials have also started using the third-generation CD28.4-1BB domain. A recent study reported a successful phase 1 and 2 trial of GD2-directed third-generation CAR-T cells for neuroblastoma (45), revealing that the third generation of CAR-T cells may be better than the second generation. In our in vitro killing experiments, B7-H3.TMI.ζ and B7-H3.28.BB.ζ CAR-T cells exhibited equivalent cytotoxicity, suggesting that TMIGD2 costimulation was equivalent to CD28.4-1BB costimulation (44). Last, comparing our lead B7-H3.TMI.ζ and B7-H3.28.BB.ζ CAR-T cell constructs, we noted that the B7-H3.TMI.ζ CAR-T cells released a lower concentration of cytokines. Given that cytokine release syndrome (CRS) may be mediated, in part, by cytokines released from CAR-T cells or cells activated by CAR-T cells (e.g., macrophages and monocytes) (46–48), TMIGD2-based CARs may represent a safer costimulatory domain as well.

In our orthotopic GBM model, but not other tumor models, we noted an unexpected toxicity in mice treated with B7-H3.28.BB.ζ CAR-T cells but not B7-H3.TMI.ζ CAR-T cells, suggesting that the latter is safer in this context. As these mice died without any substantial tumor burden, it is likely that the B7-H3.28.BB.ζ CAR-T cells rather than the tumor cells were the underlying cause. As B7-H3.28.BB.ζ CAR-T cells exhibit significantly higher levels of cytokine release than B7-H3.TMI.ζ CAR-T cells, it is possible that a localized CRS played a role in this outcome. A similar effect has been reported in the clinic, described as a "local" (49) or "compartmental" (50) CRS. This toxicity could also be magnified by the intratumoral injection of CAR-T cells in this model compared to intravenous administration in our other models.

CAR costimulatory domains have considerable impacts on CAR-T cell metabolism. CAR-T cells with a CD28 costimulatory domain use glycolytic metabolism, whereas a 4-1BB costimulatory domain uses oxidative metabolism (13). Such metabolic differences may play important roles in clinical outcomes, as a recent analysis of a CD19 CAR-T cell product from one clinical trial has demonstrated that nonresponders and partial responders show enrichment of glycolysis gene signatures (51), and analysis of cells from one patient who achieved a complete response compared to another who did not respond after CAR-NK treatment revealed oxidative phosphorylation as an up-regulated pathway (52). In our constructs, B7-H3.TMI.ζ CAR-T cells exhibited a metabolic profile less reliant on glycolysis than B7-H3.28.BB.ζ CAR-T cells based on RNA sequencing pathway analysis, ORA, acute and chronic stimulation Seahorse metabolic assays, and analysis of common DEGs between RNA sequencing experiments. Thus, our TMIGD2 domain can be used to alter CAR-T cell metabolism to a more therapeutically beneficial one.

It should be noted that, in the course of this work, most mechanistic experiments were performed using HCC827 tumors cells.

While we cannot exclude the possibility of a tumor-dependent effect, enriched RNA sequencing pathways such as "glycolysis," "oxidative phosphorylation," "Myc targets V2," and "estrogen response late" have been seen in other CAR-T cell studies (53, 54). Thus, it is likely that these and others are fundamental pathways for CAR-T cell function. Furthermore, the relationship between our CAR constructs and associated pathway analyses is complicated by the fact that detailed information on the TMIGD2 signaling pathway is only just beginning to be explored (55), so the contribution of unique or shared signaling and regulatory programs between the TMIGD2 and CD28.4-1BB costimulatory domains remains unknown. However, the transcriptional and functional differences seen in B7-H3.TMI.ζ CAR-T cells are likely due to CAR-specific maintenance of TMIGD2 signaling given that all other CAR domains were identical.

In addition to metabolic changes, we investigated whether our TMIGD2 costimulatory domain conferred other phenotypic alterations using sequencing, CAE, and in vivo approaches. Compared to B7-H3.28.BB.ζ CAR-T cells, B7-H3.TMI.ζ CAR-T cells reduced dysfunction- and exhaustion-associated phenotypes. Such programs play major roles in CAR-T cell antitumor responses (56, 57) and can be modified by the choice of costimulatory domain (10, 58, 59). Therefore, TMIGD2 costimulation is another method to prevent T cell dysfunction and exhaustion.

We also found that, upon CAE, but not during the initial generation, there was a time-dependent enrichment of central memory cells in B7-H3.TMI.ζ CAR-T cells. In vivo, B7-H3.TMI.ζ CAR-T cells also showed a larger population of central memory cells, albeit to a small degree. A higher percentage of this population is associated with better outcomes in CAR-T cell therapy (60). In addition, CAR-T cells generated from bulk CD8$^+$ T cells compared to central memory-enriched populations show an increased risk for CRS (61). Thus, our TMIGD2 costimulatory domain is an additional method to increase central memory cells and consequently may be beneficial for improving therapeutic efficacy and safety.

Last, we found an unexpected enrichment of CD8$^+$ T cells in B7-H3.TMI.ζ CAR-T cells compared to the B7-H3.28.BB.ζ CAR-T cells upon CAE. This finding was recapitulated by phenotypic analysis of in vivo lung-infiltrating T cells and reanalysis of in vivo RNA sequencing gene expression data. It has been noted in independent clinical trials that CD8$^+$ CAR-T cells make up a larger population than CD4$^+$ CAR-T cells after infusion of bulk CAR-T cell products (62) and after infusion of CAR-T cells products with a 1:1 ratio of CD8:CD4 T cells (63). In our studies, one explanation is that TMIGD2 costimulation improves the proliferation of CD8$^+$ CAR-T cells compared to CD28.4-1BB costimulation. Another explanation is that TMIGD2 costimulation improves the survival of CD8$^+$ CAR-T cells. It is also plausible that both mechanisms are at play. While our studies did not discriminate between these possibilities, it would be informative to dissect the mechanisms underlying this phenomenon.

In conclusion, we demonstrated that B7-H3 CARs incorporating a TMIGD2 costimulatory domain are effective in vitro and in vivo against multiple solid tumors. These B7-H3.TMI.ζ CAR-T cells showed several unique phenotypic changes in their metabolism, exhaustion, and memory state, which may underlie functional outcomes. Thus, B7-H3.TMI.ζ CAR-T cells are a promising approach to improve CAR-T cell therapy targeting solid tumors.

METHODS

Mice
For all in vivo experiments, 8- to 12-week-old female NSG mice were used except in fig. S7 where female and male NSG mice were used. NSG mice were purchased from the Jackson Laboratory and bred at the Albert Einstein College of Medicine (Bronx, New York). Mice were housed in a specific pathogen–free animal facility under a 12-hour light/dark cycle with food and water freely available. All experimental procedures were approved by the Albert Einstein Institutional Animal Care and Use Committee.

Cell lines
NIH 3T3 cells (mouse fibroblast), U118 cells (human GBM), HCC827 cell (human lung adenocarcinoma), THP-1 cells (human AML), AsPC-1 cells (pancreatic adenocarcinoma), Raji cells (B cell Burkitts lymphoma), PANC-1 cells (pancreatic ductal epitheloid carcinoma), and Phoenix-AMPHO cells (human epithelial kidney) were obtained from the American Type Culture Collection; NSO cells (mouse multiple myeloma) from M. Scharff (Albert Einstein College of Medicine); human embryonic kidney (HEK) 293T cells (human epithelial kidney) from W. Guo (Albert Einstein College of Medicine as a gift); and Jurkat (NFAT) cells (T cell leukemia) from BPS Bioscience. Cell lines were grown in Dulbecco's Modified Eagle's Medium or RPMI 1640 medium supplemented with 10% fetal bovine serum (FBS), 1% penicillin (100 U/ml), and 1% streptomycin (100 µg/ml) and cultured in a humidified incubator at 37°C and 5% CO_2.

Transfection of tumor cell lines
Phoenix-AMPHO cells were co-transfected with a murine stem cell virus–yellow fluorescent protein (YFP) plasmid containing the protein-of-interest [mouse B7-H3, human B7-H3, cynomolgus B7-H3, or Luciferase-tdTomato (-Luc)] and the pCMV-VSV-G plasmid using the jetPRIME transfection reagent (Polyplus) according to the manufacturer's instructions. A 48- and 72-hour viral supernatant was used to transfect tumor cell lines using polybrene (MilliporeSigma) (8 µg/ml). Transfected cells were sorted at least twice to ensure pure populations using a BD FACSAria II cell sorter.

Generation of anti–B7-H3 mAbs
A recombinant protein composed of the IgV domain of human B7-H3 fused to a human Fc fragment was generated in an inducible secreted serum-free Drosophila expression system as described previously (64) and then used for mice immunization. After immunization, hybridomas were generated by fusing NSO myeloma cells and mouse splenocytes using the standard methods as previously described (19). Antibody-producing hybridomas were screened by flow cytometry to ensure specific binding to mouse and human B7-H3. Hybridoma cells were cultured in a CELLine 350 Bioreactor Flask (DWK Life Sciences). Antibodies were purified using Protein G resin (GenScript)–packed columns. Purified B7-H3 mAbs were analyzed using SDS–polyacrylamide gel electrophoresis before affinity determination (described below), isotype determination, and variable heavy (VH) and variable light (VL) chain sequencing.

B7-H3 mAb affinity determination
Anti–B7-H3 mAb affinity to mouse and human B7-H3 was determined by BLI using the Octet RED96 system (ForteBio, Pall LLC). Recombinant mouse and human B7-H3-Fc proteins (R&D Systems) were loaded onto mouse or human capture biosensors, respectively. Afterward, the protein-loaded biosensors were placed into solutions containing serial dilutions of anti–B7-H3 mAbs. K_{on}, K_{off}, and K_D were determined by analysis using a 1:1 binding model on Octet Data Analysis software (version 9.0, ForteBio, Pall LLC).

Generation of CAR constructs
Anti–B7-H3 scFvs were generated by cloning the native mAb signal peptide sequence to the VH and VL regions of anti–B7-H3 mAbs connected by a G4S linker. The scFv was connected to a human CD8α H/TM domain, the intracellular region of various costimulatory proteins (CD28, 4-1BB, TMIGD2, CD28.4-1BB, or TMIGD2.4-1BB), followed by the intracellular domain of human CD3ζ. A self-cleaving P2A peptide sequence was then inserted, followed by the signal peptide from the granulocyte-macrophage colony-stimulating factor receptor–α chain and a truncated hEGFRt protein for CAR detection as previously described (25). For in vivo CAR-T cell persistence experiments, the hEGFRt protein was followed by a self-cleaving T2A peptide sequence, followed by a firefly luciferase gene sequence. The entire CAR sequence was cloned into the pSIN-EF2-FLAG lentiviral expression plasmid under the control of an EF1α promoter with the internal ribosomal entry site and puromycin sequences removed. A CD19.CD28,4-1BB CAR (Creative Biolabs) was also cloned into this plasmid followed by the P2A-EGFRt and T2A-Luciferase sequences described above.

Production and determination of viral titer from CAR lentivirus
HEK293T cells were co-transfected with the psPAX packaging plasmid, pMD2.G envelope plasmid, and CAR plasmid using the jetPRIME transfection reagent (Polyplus) according to the manufacturer's instructions. A 48- and 72-hour viral supernatant was collected, concentrated 100× using Lenti-X concentrator (Takara Bio) according to the manufacturer's instructions, and subsequently pooled to ensure equivalent titer. Virus titer was determined by transducing activated human T cells with the CAR lentivirus as described below. Viral titer was calculated on the basis of EGFR+ T cells.

Isolation of human T cells
Leukopaks from healthy human donors were obtained from the New York Blood Center. Peripheral blood mononuclear cells were isolated from leukopaks using density gradient centrifugation with Lymphoprep (STEMCELL Technologies) according to the manufacturer's instructions. T cells were purified using a T cell negative enrichment kit (BD Biosciences) according to the manufacturer's instructions. T cells were either frozen in freezing medium (90% FBS and 10% dimethyl sulfoxide) and stored in liquid nitrogen or were used immediately.

Generation of CAR-T cells
Fresh or thawed T cells were activated for 24 hours on an OKT3 (1 µg/ml) and CD28 (1 µg/ml) antibody-coated 24-well plate in CTS OpTmizer medium (Gibco) supplemented with OpTmizer T cell expansion supplement, 10% FBS, 1% ʟ-glutamine (200 mM), 1% penicillin (100 U/ml), 1% streptomycin (100 µg/ml), IL-7 (10 ng/ml), and IL-15 (5 ng/ml). Activated T cells were then transduced on non–tissue culture–treated plates coated with RetroNectin reagent (Takara Bio) (19 µg/ml) and CAR lentivirus (multiplicity of infection of approximately 10) according to the manufacturer's instructions. CAR-T cells were then expanded for at least 7 days

before use in experiments. Before all experiments, CAR-T cell transduction efficiency was normalized to 50% CAR$^+$ cells (for in vitro cytotoxicity screening assay) or to the lowest efficiency donor by adding of non-transduced T cells. If necessary, CAR-T cells were purified using anti-phycoerythrin (PE) microbeads (Miltenyi Biotec) following anti-EGFR-PE staining according to the manufacturer's instructions.

In vitro coculture killing assays

CAR-T cells (0.1×10^6) and either HCC827-Luc cells (0.01×10^6), U118-Luc cells (0.01×10^6), or THP-1 cells (0.1×10^6) were plated in duplicate in T cell medium without the addition of cytokines. Three to 5 days later, the tumor cells were enumerated using Count-Bright absolute counting beads (Thermo Fisher Scientific) with flow cytometry. For the Incucyte (Sartorius) time-lapse cytotoxicity assays, 5×10^3 HCC827-Luc or U118-Luc cells were plated 1 day before imaging. Tumor-coated plates were then placed in the Incucyte machine and imaged every 4 hours at four locations per well for a total of 112 hours. Sixteen hours after the initial imaging, 0.1×10^6 CAR-T cells were gently added to the wells. Imaging data were analyzed using the Incucyte software (Sartorius).

Flow cytometry

Cells were stained at room temperature or 4°C for 15 to 30 min using antibodies conjugated to the following fluorophores: fluorescein isothiocyanate, PE, allophycocyanin (APC), APC-Fire 750, PE-cyanine (Cy)7, peridinin-chlorophyll-protein–Cy5.5, brilliant violet (BV)–421, BV-711, Alexa Fluor (AF)–532, AF-488, brilliant ultra violet (BUV)–496, BUV-395, BUV-496, and BUV-737. Expression of tdTomato and YFP was also used to distinguish cell populations. Antibody targets include CD45, CD3, CD4, CD8, CD45RA, CCR7, EGFR, G4S linker, PD-1, TIM-3, LAG-3, B7-H3, CD69, CD19, CD33, HK1, ALDOA, PFKFB3, SLC16A3, and rabbit antibody. Viability was determined using 7-amino-actinomycin D, zombieNIR, ghost violet 510, and 4′,6-diamidino-2-phenylindole. In some experiments, cells were fixed using a 2% paraformaldehyde solution before analysis. All samples were acquired using a BD LSRII or Cytek Aurora flow cytometer. Data analysis was performed on FlowJo (BD Biosciences) or SpectroFlo (Cytek Biosciences) software. t-SNE plots were generated using the t-SNE plugin on FlowJo.

Glycolysis-associated protein quantification

CAR-T cells (0.1×10^6) were cocultured with 0.1×10^5 HCC827-Luc tumor cells in 96-well plates in duplicate or triplicate as described above. After 72 hours, CAR-T cells were collected and stained with a fixable viability dye (Zombie NIR or ghost violet 510) and fluorophore-conjugated CD3 and EGFR as described above. CAR-T cells were fixed and permeabilized in fixation/permeabilization solution (BD Biosciences) according to the manufacturer's instructions; washed with permeabilization/wash buffer (BD Biosciences) according to the manufacturer's instructions; and incubated in unconjugated primary rabbit anti-human MCT4, HK1, ALDOA, or PFKFB3 for 15 to 30 min at room temperature. Afterward, the CAR-T cells were washed with permeabilization/wash buffer and incubated in fluorophore-conjugated anti-rabbit antibody for 15 to 30 min at room temperature. Cells were washed in permeabilization/wash buffer and analyzed using a Cytek Aurora flow cytometer.

Flow cytometry cytokine analysis

CAR-T cells (0.4×10^6) and HCC827 tumor cells (0.1×10^6) were cocultured for 24 hours in 24-well plates. Supernatants from the cocultures were collected and stored at −80°C until analysis. The concentration of IL-2, IL-4, IL-5, IL-6, IL-9, IL-10, IL-13, IL-17A, IL-17F, IL-22, IFN-γ, and TNF-α was determined using the flow cytometry–based LEGENDplex human Th cytokine panel kit (BioLegend) according to the manufacturer's instructions on nondiluted or 1:5 diluted supernatant samples. Data were analyzed using the LEGENDplex online data analysis software suite.

RNA isolation

For in vitro RNA isolation, CAR-T cells were gently removed from coculture wells and plated into fresh wells for 30 min to allow excess tumor cells to attach to the plate. CAR-T cells were gently removed once more, and live cells were enriched using Lymphoprep (STEMCELL Technologies) density gradient centrifugation according to the manufacturer's instructions. T cells were further purified isolated using a CD3$^+$ selection beads (Miltenyi Biotec). RNA was extracted using the RNeasy Plus Mini Kit (Qiagen) and stored at −80°C. RNA sequencing (40 million paired-end reads) after library preparation (using the NEBNext Ultra II kit) was performed by Admera Health. For in vivo RNA isolation, lung-infiltrating T cells were isolated from mouse lungs. Briefly, single-cell suspensions were prepared from lungs by enzymatic digestion [collagenase IV (200 IU/ml; Gibco), dispase (0.5 IU/ml), and deoxyribonuclease I (100 U/ml)] in RPMI 1640 medium. Next, the single-cell suspension was layered on a discontinuous density gradient Percoll solutions (40 and 80%), and the immune cells at the 40% 80% interface were collected. A second density gradient centrifugation using Lymphoprep was performed to further enrich the live cell population. Mouse cells were then depleted two times using a mouse cell removal kit (Miltenyi Biotec). Afterward, T cells from the same donor transduced with the same CAR were pooled, and RNA was isolated as described above. RNA sequencing (40 million paired-end reads) after library preparation (using the SMARTseq V4 with NExtera XT kit) was performed by Admera Health.

B7-H3 CAR versus CD19 CAR RNA sequencing analysis

Paired-end reads from RNA sequencing were aligned using the STAR alignment software (version 2.6.1b) (65) to a reference human genome (hg38). Gene-mapped fragments were counted using HTseq software (version 0.6.1) (66). Genes with an average expression count of ≥1 in either group were considered expressed and used for differential expression analysis, with significance of changes set to an adjusted P value of <0.05 and absolute log$_2$ fold change of >0.5. Principal components analysis and differential expression analysis were performed using the DESeq2 software (version 1.3.10) (67). GSEA was performed using the Hallmark and Reactome databases using ranked gene lists determined by multiplying the −log$_{10}$ P value and the sign of the log$_2$(fold change) (68).

B7-H3 CAR in vitro and in vivo RNA sequencing analysis

Paired-end reads from RNA sequencing were aligned using the STAR aligner (version 2.7.9a) (65) to the human reference genome (hg38). The alignment data were then used by the RSEM software (version 1.3.3) (69) to quantify expression levels of individual genes (both coding and non-coding) in the GENCODE annotation (version 41), yielding estimated read counts and transcripts per

million (TPMs). Genes with a TPM < 1 in all samples were excluded from further analysis. DEGs were determined by an adjusted P value of <0.05 and $\log_2$ fold change of >0.5, using the DESeq2 software (version 1.38.3) (67). GSEA was performed using the Hallmark and Reactome databases using ranked gene lists determined by multiplying the $-\log P$ value and the $\log_2$ fold change (68). Gene sets with a false discovery rate < 0.05 were considered enriched. Function ORA was also performed on DEGs with a >1.5 fold expression change and adjusted P value of <0.05 using the Cluster Profiler (version 4.6.2) enrichGO function. Pathways with an adjusted P value of <0.05 were considered enriched in either the up- or down-regulated genes. Gene sets describing T cell dysfunction (32) and metabolism (29) were obtained from the literature, and the inhibitory protein list was manually curated; these gene lists are available in table S7.

Seahorse metabolic assay

CAR-T cells (0.1×10^6) were cocultured alone or with 5×10^3 HCC827 tumor cells for 1 or 7 days with tumor addback. CAR-T cells were then gently collected from the wells and transferred to an unused well for 30 min to allow for attachment of any tumor cells. CAR-T cells were then gently recollected and analyzed using the Seahorse T cell metabolic profiling kit (Agilent) or Seahorse Substrate oxidation stress test kits (Agilent) on Seahorse Poly-D-Lysine (PDL)-coated plates (Agilent), and, according to the manufacturer's instructions with one slight modification, after transfer to PDL-coated plates, CAR-T cells were rested 5 min before centrifugation to allow for even cell distribution on the bottom of the well. Seahorse plates were run on a Seahorse XF96 analyzer (Agilent) with three to six measurements taken after 3 min of mixing and 3 min of recording at baseline and after injections of Etomoxir, UK5009, BPTES, oligomycin A, Bam15, and rotenone/antimycin A. Data were analyzed using Agilent Seahorse Analytics online software. %ATP from mitochondria was obtained by the following formula: $100\% - \%\text{ATP from glycolysis}$.

Jurkat (NFAT) T cell activation experiment

Jurkat (NFAT) cells were transduced with CAR constructs as described above. Triplicate wells in a 96-well plate were coated with either OKT3 (1 µg/ml) or 0.2×10^5 tumor cells (U118, HCC827, or AsPC-1) overnight. The following day, the wells were washed with phosphate-buffered saline (PBS), and fresh T cell medium was added. Raji tumor cells (0.2×10^5) were added to additional triplicate wells. Non-transduced or CAR-transduced Jurkat (NFAT) cells (0.1×10^6) were added to each well and incubated for 6 hours. The Bio-Glo Luciferase assay system (Promega) was then used to detect the Jurkat (NFAT) luciferase according to the manufacturer's instructions. Luciferase signal was acquired on a plate reader (PerkinElmer).

Chronic antigen exposure

The CAE experiment was modified from a previously described protocol (32). Briefly, 0.2×10^6 CAR-T cells were plated in 96-well plates in triplicate wells using T cell medium without cytokines. HCC827 tumor cells (0.1×10^5) were then added to each well. Every 3 to 4 days, CAR-T cells were gently removed from the well and transferred to an unused well. A small-cell aliquot was then analyzed using flow cytometry. Unanalyzed CAR-T cells were centrifuged, and additional supernatant was removed such that one-half

of the original volume remained in the well. HCC827 parental cells (0.1×10^5) in fresh T cell medium were then added at an equivalent volume. This process was repeated for a total of 17 days.

Bioluminescent imaging

Bioluminescent imaging was performed using the IVIS Spectrum in vivo imaging system (PerkinElmer) and analyzed using Living Image software (version 3.0). Images were acquired 10 to 15 min after intraperitoneal injection of D-luciferin (Gold Biotechnology) (150 µg/g of mouse weight).

In vivo lung cancer model

HCC827-Luc cells (0.5×10^6) were injected intravenously in the lateral tail vein of NSG mice in 100 µl of sterile PBS. Three days later, tumor engraftment was confirmed via IVIS imaging, and experimental groups were normalized to ensure equivalent baseline tumor burden. One injection of 10×10^6 CAR-T cells was then given intravenously into the lateral tail vein, followed by an additional injection 1 week later. Tumor burden was tracked via IVIS imaging over the course of 101 days. Survival was also tracked during this time.

In vivo GBM model

U118-Luc tumor cells were resuspended at 5×10^3 cells/µl in sterile PBS. A small hole was drilled in the skull using an 18-gauge needle 1 mm lateral and 1 mm anterior to bregma using the freehand method (70) in NSG mice anesthetized with continuous isoflurane (2%). Tumor cells (2 µl) were then slowly injected into the hole perpendicular to the benchtop surface using a blunt end Hamilton syringe fitted with a sterile precut pipette tip that exposed 1 mm of the syringe needle over the course of 1 min. The syringe injection apparatus was left in place for 30 s and then slowly removed. The surgical site was then closed using autoclips (Thermo Fisher Scientific). Meloxicam (5 mg/kg) was administered preemptively and for 2 days after tumor implantation. Seven days later, the autoclips were removed, and tumor engraftment was confirmed using IVIS imaging. Mice were then allocated into experimental groups normalized for baseline tumor burden. Afterward, 1×10^6 CAR-T cells were injected intratumorally using the same surgical preparation described above in a 2-µl volume of PBS. Tumor burden was tracked via IVIS imaging for 100 days. Survival was tracked during this time.

In vivo pancreatic cancer model

PANC-1-Luc tumor cells were resuspended at 1×10^4 cells/50 µl of sterile PBS. The pancreas was expressed though a 1-cm incision made in the skin and musculature of NSG mice anesthetized with continuous isoflurane (2%). Tumor cells (50 µl) were injected slowly into the head of the pancreas over the course of 30 s using a 27-gauge needle (Becton Dickinson). The needle was left for 30 s and then slowly removed using a twirling motion. The musculature was closed using with 5-0 dissolvable suture (Stoelting) in a simple uninterrupted pattern, and the skin was closed with autoclips. Meloxicam was administered preemptively and for 3 days after tumor implantation. Seven days later, tumor engraftment was confirmed using IVIS imaging. Mice were then allocated into experimental groups normalized for baseline tumor burden. CAR-T cells (10×10^6) were then injected intravenously into the lateral tail vein, followed by another injection 7 days later. Tumor burden was tracked via IVIS imaging for 100 days. Survival was simultaneously tracked as well.

In vivo subcutaneous tumor model

HCC827 tumor cells (10×10^6) were subcutaneously injected into the right flank of NSG mice in 50 μl of sterile PBS. After 2 weeks, tumor engraftment was confirmed by caliper measurement, and experimental groups were normalized to ensure an equivalent baseline tumor burden. CAR-T cells (10×10^6) were intratumorally injected in 50 μl of sterile PBS. Seven to 8 days later, the mice were euthanized to analyze tumor-infiltrating CAR-T cells.

In vivo CAR-T cell persistence model

Parental HCC827 tumor cells (0.5×10^6) were intravenously injected into the lateral tail vein in a 100-μl volume of sterile PBS. Three days later, a single dose of 10×10^6 CAR-Luc T cells was injected intravenously into the lateral tail vein. CAR-Luc T cell signal was tracked using IVIS imaging over the course of 46 days.

Immune cell isolation from mouse blood, organs, and subcutaneous tumors

To obtain immune cells from mouse blood, blood was taken from the lateral tail vein in heparinized capillary tubes (Thermo Fisher Scientific). Red blood cells (RBCs) were then lyzed using RBC lysis buffer (Tonbo) according the manufacturer's instructions. Remaining cells were then washed twice with PBS before flow cytometry analysis. To obtain immune cells from organs, mice were first euthanized. Organs of interest were directly removed (spleens) or perfused with PBS and then removed (lungs), then weighed, and stored in ice cold PBS. Spleens were then transferred to C tubes (Miltenyi Biotec) and mechanically dissociated using the gentleMACs Dissociator (Milenyi Biotec). The cell suspension was strained through a 40-μm filter. The remaining cells were then washed twice in PBS before flow cytometry analysis. To obtain immune cells from the lungs, single-cell suspensions were made using enzymatic digestion as described above, and immune cells isolated using discontinuous Percoll gradients as described above. RBC lysis buffer was performed to remove RBCs, and the remaining cells were then washed twice in PBS before flow cytometry analysis. To obtain immune cells from subcutaneous tumors, tumors were excised and single-cell suspensions were made using a human tumor dissociation kit (Miltenyi Biotec) according to the manufacturer's instructions. The single-cell suspension was then layered on a discontinuous Percoll gradients as described above to obtain immune cells. The cells were then washed twice in PBS before flow cytometry staining and analysis within 12 hours.

Statistics

Statistical analysis was performed using GraphPad prism software (version 9.4.1). As described in each figure legend, testing between groups was performed using an unpaired two-tailed Student's t test, one-way analysis of variance (ANOVA) with Tukey's multiple comparison's test, Kruskal-Wallis test, two-way ANOVA with Tukey's or Šídák's multiple comparisons test, or Mantel-Cox log-rank test. The data are shown as individual values or as individual values and the means $\pm$ SEM. A P value of less than 0.05 was considered statistically significant.

Supplementary Materials

This PDF file includes:
Figs. S1 to S10
Legends for tables S1 to S9

Other Supplementary Material for this manuscript includes the following:
Tables S1 to S9

REFERENCES AND NOTES

1. S. S. Neelapu, F. L. Locke, N. L. Bartlett, L. J. Lekakis, D. B. Miklos, C. A. Jacobson, I. Braunschweig, O. O. Oluwole, T. Siddiqi, Y. Lin, J. M. Timmerman, P. J. Stiff, J. W. Friedberg, I. W. Flinn, A. Goy, B. T. Hill, M. R. Smith, A. Deol, U. Farooq, P. McSweeney, J. Munoz, I. Avivi, J. E. Castro, J. R. Westin, J. C. Chavez, A. Ghobadi, K. V. Komanduri, R. Levy, E. D. Jacobsen, T. E. Witzig, P. Reagan, A. Bot, J. Rossi, L. Navale, Y. Jiang, J. Aycock, M. Elias, D. Chang, J. Wiezorek, W. Y. Go, Axicabtagene ciloleucel CAR T-cell therapy in refractory large B-cell lymphoma. *N. Engl. J. Med.* **377**, 2531–2544 (2017).

2. T. W. Laetsch, S. L. Maude, S. Rives, H. Hiramatsu, H. Bittencourt, P. Bader, A. Baruchel, M. Boyer, B. De Moerloose, M. Qayed, J. Buechner, M. A. Pulsipher, G. D. Myers, H. E. Stefanski, P. L. Martin, E. Nemecek, C. Peters, G. Yanik, S. L. Khaw, K. L. Davis, J. Krueger, A. Balduzzi, N. Boissel, R. Tiwari, D. O'Donovan, S. A. Grupp, Three-year update of tisagenlecleucel in pediatric and young adult patients with relapsed/refractory acute lymphoblastic leukemia in the ELIANA trial. *J. Clin. Oncol.* **41**, 1664–1669 (2023).

3. P. Rodriguez-Otero, S. Ailawadhi, B. Arnulf, K. Patel, M. Cavo, A. K. Nooka, S. Manier, N. Callander, L. J. Costa, R. Vij, N. J. Bahlis, P. Moreau, S. R. Solomon, M. Delforge, J. Berdeja, A. Truppel-Hartmann, Z. Yang, L. Favre-Kontula, F. Wu, J. Piasecki, M. Cook, S. Giralt, Ide-cel or standard regimens in relapsed and refractory multiple myeloma. *N. Engl. J. Med.* **388**, 1002–1014 (2023).

4. Y.-J. Chen, B. Abila, Y. Mostafa Kamel, CAR-T: What is next? *Cancers* **15**, 663 (2023).

5. D. M. O'Rourke, M. P. Nasrallah, A. Desai, J. J. Melenhorst, K. Mansfield, J. J. D. Morrissette, M. Martinez-Lage, S. Brem, E. Maloney, A. Shen, R. Isaacs, S. Mohan, G. Plesa, S. F. Lacey, J.-M. Navenot, Z. Zheng, B. L. Levine, H. Okada, C. H. June, J. L. Brogdon, M. V. Maus, A single dose of peripherally infused EGFRvIII-directed CAR T cells mediates antigen loss and induces adaptive resistance in patients with recurrent glioblastoma. *Sci. Transl. Med.* **9**, eaaa0984 (2017).

6. S. L. Goff, R. A. Morgan, J. C. Yang, R. M. Sherry, P. F. Robbins, N. P. Restifo, S. A. Feldman, Y. C. Lu, L. Lu, Z. Zheng, L. Xi, M. Epstein, L. S. McIntyre, P. Malekzadeh, M. Raffeld, H. A. Fine, S. A. Rosenberg, Pilot trial of adoptive transfer of chimeric antigen receptor-transduced T cells targeting EGFRvIII in patients with glioblastoma. *J. Immunother.* **42**, 126–135 (2019).

7. M. H. Kershaw, J. A. Westwood, L. L. Parker, G. Wang, Z. Eshhar, S. A. Mavroukakis, D. E. White, J. R. Wunderlich, S. Canevari, L. Rogers-Freezer, C. C. Chen, J. C. Yang, S. A. Rosenberg, P. Hwu, A phase I study on adoptive immunotherapy using gene-modified T cells for ovarian cancer. *Clin. Cancer Res.* **12**, 6106–6115 (2006).

8. C. Zhang, Z. Wang, Z. Yang, M. Wang, S. Li, Y. Li, R. Zhang, Z. Xiong, Z. Wei, J. Shen, Y. Luo, Q. Zhang, L. Liu, H. Qin, W. Liu, F. Wu, W. Chen, F. Pan, X. Zhang, P. Bie, H. Liang, G. Pecher, C. Qian, Phase I escalating-dose trial of CAR-T therapy targeting CEA$^+$ metastatic colorectal cancers. *Mol. Ther.* **25**, 1248–1258 (2017).

9. R. Weinkove, P. George, N. Dasyam, A. D. McLellan, Selecting costimulatory domains for chimeric antigen receptors: Functional and clinical considerations. *Clin. Transl. Immunology* **8**, e1049 (2019).

10. A. H. Long, M. Haso, J. F. Shern, K. M. Wanhainen, M. Murgai, M. Ingaramo, J. P. Smith, A. J. Walker, M. E. Kohler, V. R. Venkateshwara, R. N. Kaplan, G. H. Patterson, T. J. Fry, R. J. Orentas, C. L. Mackall, 4-1BB costimulation ameliorates T cell exhaustion induced by tonic signaling of chimeric antigen receptors. *Nat. Med.* **21**, 581–590 (2015).

11. Z. Ying, T. He, X. Wang, W. Zheng, N. Lin, M. Tu, Y. Xie, L. Ping, C. Zhang, W. Liu, L. Deng, F. Qi, Y. Ding, X.-A. Lu, Y. Song, J. Zhu, Parallel comparison of 4-1BB or CD28 co-stimulated CD19-targeted CAR-T cells for B cell non-Hodgkin's lymphoma. *Mol. Ther. Oncolytics* **15**, 60–68 (2019).

12. D. Nehama, N. Di Ianni, S. Musio, H. Du, M. Patane, B. Pollo, G. Finocchiaro, J. J. H. Park, D. E. Dunn, D. S. Edwards, J. S. Damrauer, H. Hudson, S. R. Floyd, S. Ferrone, B. Savoldo, S. Pellegatta, G. Dotti, B7-H3-redirected chimeric antigen receptor T cells target glioblastoma and neurospheres. *EBioMedicine* **47**, 33–43 (2019).

13. O. U. Kawalekar, R. S. O'Connor, J. A. Fraietta, L. Guo, S. E. McGettigan, A. D. Posey Jr., P. R. Patel, S. Guedan, J. Scholler, B. Keith, N. W. Snyder, I. A. Blair, M. C. Milone, C. H. June, Distinct signaling of coreceptors regulates specific metabolism pathways and impacts memory development in CAR T cells. *Immunity* **44**, 380–390 (2016).

14. E. Drent, R. Poels, R. Ruiter, N. W. C. J. van de Donk, S. Zweegman, H. Yuan, J. de Bruijn, M. Sadelain, H. M. Lokhorst, R. W. J. Groen, T. Mutis, M. Themeli, Combined CD28 and 4-1BB costimulation potentiates affinity-tuned chimeric antigen receptor-engineered T cells. *Clin. Cancer Res.* **25**, 4014–4025 (2019).

15. X. Zhao, J. Yang, X. Zhang, X. A. Lu, M. Xiong, J. Zhang, X. Zhou, F. Qi, J. He, Y. Ding, X. Hu, F. De Smet, P. Lu, X. Huang, Efficacy and safety of CD28- or 4-1BB-based CD19 CAR-T cells in B cell acute lymphoblastic leukemia. *Mol. Ther. Oncolytics* **18**, 272–281 (2020).

16. Y. Wei, X. Ren, P. M. Galbo Jr., S. Moerdler, H. Wang, R. A. Sica, B. Etemad-Gilbertson, L. Shi, L. Zhu, X. Tang, Q. Lin, M. Peng, F. Guan, D. Zheng, J. M. Chinai, X. Zang, KIR3DL3-HHLA2 is a human immunosuppressive pathway and a therapeutic target. *Sci. Immunol.* **6**, eabf9792 (2021).

17. M. C. Pulanco, A. T. Madsen, A. Tanwar, D. T. Corrigan, X. Zang, Recent advancements in the B7/CD28 immune checkpoint families: New biology and clinical therapeutic strategies. *Cell. Mol. Immunol.* **20**, 694–713 (2023).

18. M. Janakiram, J. M. Chinai, S. Fineberg, A. Fiser, C. Montagna, R. Medavarapu, E. Castano, H. Jeon, K. C. Ohaegbulam, R. Zhao, A. Zhao, S. C. Almo, J. A. Sparano, X. Zang, Expression, clinical significance, and receptor identification of the newest B7 family member HHLA2 protein. *Clin. Cancer Res.* **21**, 2359–2366 (2015).

19. R. Zhao, J. M. Chinai, S. Buhl, L. Scandiuzzi, A. Ray, H. Jeon, K. C. Ohaegbulam, K. Ghosh, A. Zhao, M. D. Scharff, X. Zang, HHLA2 is a member of the B7 family and inhibits human CD4 and CD8 T-cell function. *Proc. Natl. Acad. Sci. U.S.A.* **110**, 9879–9884 (2013).

20. Y. Zhu, S. Yao, B. P. Iliopoulou, X. Han, M. M. Augustine, H. Xu, R. T. Phennicie, S. J. Flies, M. Broadwater, W. Ruff, J. M. Taube, L. Zheng, L. Luo, G. Zhu, J. Chen, L. Chen, B7-H5 costimulates human T cells via CD28H. *Nat. Commun.* **4**, 2043 (2013).

21. Y. Tian, Y. Sun, F. Gao, M. R. Koenig, A. Sunderland, Y. Fujiwara, R. J. Torphy, L. Chen, B. H. Edil, R. D. Schulick, Y. Zhu, CD28H expression identifies resident memory CD8 + T cells with less cytotoxicity in human peripheral tissues and cancers. *Oncoimmunology* **8**, e1538440 (2019).

22. J. Crespo, L. Vatan, T. Maj, R. Liu, I. Kryczek, W. Zou, Phenotype and tissue distribution of CD28H+ immune cell subsets. *Oncoimmunology* **6**, e1362529 (2017).

23. E. Picarda, K. C. Ohaegbulam, X. Zang, Molecular pathways: Targeting B7-H3 (CD276) for human cancer immunotherapy. *Clin. Cancer Res.* **22**, 3425–3431 (2016).

24. V. Vigdorovich, U. A. Ramagopal, E. Lázár-Molnár, E. Sylvestre, J. S. Lee, K. A. Hofmeyer, X. Zang, S. G. Nathenson, S. C. Almo, Structure and T cell inhibition properties of B7 family member, B7-H3. *Structure* **21**, 707–717 (2013).

25. X. Wang, W. C. Chang, C. W. Wong, D. Colcher, M. Sherman, J. R. Ostberg, S. J. Forman, S. R. Riddell, M. C. Jensen, A transgene-encoded cell surface polypeptide for selection, in vivo tracking, and ablation of engineered cells. *Blood* **118**, 1255–1263 (2011).

26. J. Y. Spiegel, S. Patel, L. Muffly, N. M. Hossain, J. Oak, J. H. Baird, M. J. Frank, P. Shiraz, B. Sahaf, J. Craig, M. Iglesias, S. Younes, Y. Natkunam, M. G. Ozawa, E. Yang, J. Tamaresis, H. Chinnasamy, Z. Ehlinger, W. Reynolds, R. Lynn, M. C. Rotiroti, N. Gkitsas, S. Arai, L. Johnston, R. Lowsky, R. G. Majzner, E. Meyer, R. S. Negrin, A. R. Rezvani, S. Sidana, J. Shizuru, W.-K. Weng, C. Mullins, A. Jacob, I. Kirsch, M. Bazzano, J. Zhou, S. Mackay, S. J. Bornheimer, L. Schultz, S. Ramakrishna, K. L. Davis, K. A. Kong, N. N. Shah, H. Qin, T. Fry, S. Feldman, C. L. Mackall, D. B. Miklos, CAR T cells with dual targeting of CD19 and CD22 in adult patients with recurrent or refractory B cell malignancies: A phase 1 trial. *Nat. Med.* **27**, 1419–1431 (2021).

27. Y. Zhang, C. Li, M. Du, H. Jiang, W. Luo, L. Tang, Y. Kang, J. Xu, Z. Wu, X. Wang, Z. Huang, Y. Zhang, D. Wu, A. H. Chang, Y. Hu, H. Mei, Allogenic and autologous anti-CD7 CAR-T cell therapies in relapsed or refractory T-cell malignancies. *Blood Cancer J.* **13**, 61 (2023).

28. J. Theruvath, E. Sotillo, C. W. Mount, C. M. Graef, A. Delaidelli, S. Heitzeneder, L. Labanieh, S. Dhingra, A. Leruste, R. G. Majzner, P. Xu, S. Mueller, D. W. Yecies, M. A. Finetti, D. Williamson, P. D. Johann, M. Kool, S. Pfister, M. Hasselblatt, M. C. Frühwald, O. Delattre, D. Surdez, F. Bourdeaut, S. Puget, S. Zaidi, S. S. Mitra, S. Cheshier, P. H. Sorensen, M. Monje, C. L. Mackall, Locoregionally administered B7-H3-targeted CAR T cells for treatment of atypical teratoid/rhabdoid tumors. *Nat. Med.* **26**, 712–719 (2020).

29. M. Frederick, H. D. Skinner, S. A. Kazi, A. G. Sikora, V. C. Sandulache, High expression of oxidative phosphorylation genes predicts improved survival in squamous cell carcinomas of the head and neck and lung. *Sci. Rep.* **10**, 6380 (2020).

30. P. J. Ahl, R. A. Hopkins, W. W. Xiang, B. Au, N. Kaliaperumal, A.-M. Fairhurst, J. E. Connolly, Met-Flow, a strategy for single-cell metabolic analysis highlights dynamic changes in immune subpopulations. *Commun. Biol.* **3**, 305 (2020).

31. L. A. K. Fonkoua, O. Sirpilla, R. Sakemura, E. L. Siegler, S. S. Kenderian, CAR T cell therapy and the tumor microenvironment: Current challenges and opportunities. *Mol. Ther. Oncolytics* **25**, 69–77 (2022).

32. C. R. Good, M. A. Aznar, S. Kuramitsu, P. Samareh, S. Agarwal, G. Donahue, K. Ishiyama, N. Wellhausen, A. K. Rennels, Y. Ma, L. Tian, S. Guedan, K. A. Alexander, Z. Zhang, P. C. Rommel, N. Singh, K. M. Glastad, M. W. Richardson, K. Watanabe, J. Tanyi, M. H. O'Hara, M. Ruella, S. F. Lacey, E. K. Moon, S. J. Schuster, S. M. Albelda, L. L. Lanier, R. M. Young, S. L. Berger, C. H. June, An NK-like CAR T cell transition in CAR T cell dysfunction. *Cell* **184**, 6081–6100.e26 (2021).

33. E. Schoutrop, T. Poiret, I. El-Serafi, Y. Zhao, R. He, A. Moter, J. Henriksson, M. Hassan, I. Magalhaes, J. Mattsson, Tuned activation of MSLN-CAR T cells induces superior antitumor responses in ovarian cancer models. *J. Immunother. Cancer* **11**, e005691 (2023).

34. M. E. Selli, J. H. Landmann, M. Terekhova, J. Lattin, A. Heard, Y. S. Hsu, T. C. Chang, J. Chang, J. Warrington, H. Ha, N. Kingston, G. Hogg, M. Slade, M. M. Berrien-Elliott, M. Foster, S. Kersting-Schadek, A. Gruszczynska, D. DeNardo, T. A. Fehniger, M. Artyomov, N. Singh, Costimulatory domains direct distinct fates of CAR-driven T-cell dysfunction. *Blood* **141**, 3153–3165 (2023).

35. W. Li, S. Qiu, J. Chen, S. Jiang, W. Chen, J. Jiang, F. Wang, W. Si, Y. Shu, P. Wei, G. Fan, R. Tian, H. Wu, C. Xu, H. Wang, Chimeric antigen receptor designed to prevent ubiquitination and downregulation showed durable antitumor efficacy. *Immunity* **53**, 456–470.e6 (2020).

36. S. Ghassemi, J. S. Durgin, S. Nunez-Cruz, J. Patel, J. Leferovich, M. Pinzone, F. Shen, K. D. Cummins, G. Plesa, V. A. Cantu, S. Reddy, F. D. Bushman, S. I. Gill, U. O'Doherty,

37. R. S. O'Connor, M. C. Milone, Rapid manufacturing of non-activated potent CAR T cells. *Nat. Biomed. Eng.* **6**, 118–128 (2022).

37. T. Tokatlian, G. E. Asuelime, J.-Y. Mock, B. DiAndreth, S. Sharma, D. Toledo Warshaviak, M. E. Daris, K. Bolanos, B. L. Luna, M. S. Naradikian, K. Deshmukh, A. E. Hamburger, A. Kamb, Mesothelin-specific CAR-T cell therapy that incorporates an HLA-gated safety mechanism selectively kills tumor cells. *J. Immunother. Cancer* **10**, e003826 (2022).

38. S. Solouki, W. Huang, J. Elmore, C. Limper, F. Huang, A. August, TCR signal strength and antigen affinity regulate CD8+ memory T cells. *J. Immunol.* **205**, 1217–1227 (2020).

39. M. Shakiba, P. Zumbo, G. Espinosa-Carrasco, L. Menocal, F. Dündar, S. E. Carson, E. M. Bruno, F. J. Sanchez-Rivera, S. W. Lowe, S. Camara, R. P. Koche, V. P. Reuter, N. D. Socci, B. Whitlock, F. Tamzalit, M. Huse, M. D. Hellmann, D. K. Wells, N. A. Defranoux, D. Betel, M. Philip, A. Schietinger, TCR signal strength defines distinct mechanisms of T cell dysfunction and cancer evasion. *J. Exp. Med.* **219**, e20201966 (2021).

40. G. Hu, G. Li, W. Wen, W. Ding, Z. Zhou, Y. Zheng, T. Huang, J. Ren, R. Chen, D. Zhu, R. He, Y. Liang, M. Luo, Case report: B7-H3 CAR-T therapy partially controls tumor growth in a basal cell carcinoma patient. *Front. Oncol.* **12**, 956593 (2022).

41. X. Tang, F. Liu, Z. Liu, Y. Cao, Z. Zhang, Y. Wang, J. Huang, S. Fan, S. Zhao, Y. Chen, G. Li, S. Wang, M. Zheng, Y. Hu, H. Li, C. Jiang, M. Yang, H. Yang, J. Xu, G. Guo, A. Tong, L. Zhou, Bioactivity and safety of B7-H3-targeted chimeric antigen receptor T cells against anaplastic meningioma. *Clin. Transl. Immunol.* **9**, e1137 (2020).

42. X. Tang, Y. Wang, J. Huang, Z. Zhang, F. Liu, J. Xu, G. Guo, W. Wang, A. Tong, L. Zhou, Administration of B7-H3 targeted chimeric antigen receptor-T cells induce regression of glioblastoma. *Signal Transduct. Target. Ther.* **6**, 125 (2021).

43. N. R. Pinto, C. M. Albert, M. Taylor, A. Wilson, S. Rawlings-Rhea, W. Huang, K. Seidel, P. Narayanaswamy, V. Wu, C. Brown, N. A. Vitanza, R. Orentas, R. A. Gardner, M. C. Jensen, J. R. Park, STRIVE-02: A first-in-human phase 1 trial of systemic B7H3 CAR T cells for children and young adults with relapsed/refractory solid tumors. *J. Clin. Oncol.* **40**, 10011 (2022).

44. S. Gill, J. N. Brudno, CAR T-cell therapy in hematologic malignancies: Clinical role, toxicity, and unanswered questions. *Am. Soc. Clin. Oncol. Educ. Book* **41**, e246–e265 (2021).

45. F. Del Bufalo, B. De Angelis, I. Caruana, G. Del Baldo, M. A. De Ioris, A. Serra, A. Mastronuzzi, M. G. Cefalo, D. Pagliara, M. Amicucci, G. Li Pira, G. Leone, V. Bertaina, M. Sinibaldi, S. Di Cecca, M. Guercio, Z. Abbaszadeh, L. Iaffaldano, M. Gunetti, S. Iacovelli, R. Bugianesi, S. Macchia, M. Algeri, P. Merli, F. Galaverna, R. Abbas, M. C. Garganese, M. F. Villani, G. S. Colafati, F. Bonetti, M. Rabusin, K. Perruccio, V. Folsi, C. Quintarelli, F. Locatelli, GD2-CART01 for relapsed or refractory high-risk neuroblastoma. *N. Engl. J. Med.* **388**, 1284–1295 (2023).

46. X. Xiao, S. Huang, S. Chen, Y. Wang, Q. Sun, X. Xu, Y. Li, Mechanisms of cytokine release syndrome and neurotoxicity of CAR T-cell therapy and associated prevention and management strategies. *J. Exp. Clin. Cancer Res.* **40**, 367 (2021).

47. T. Giavridis, S. J. C. van der Stegen, J. Eyquem, M. Hamieh, A. Piersigilli, M. Sadelain, CAR T cell-induced cytokine release syndrome is mediated by macrophages and abated by IL-1 blockade. *Nat. Med.* **24**, 731–738 (2018).

48. M. Norelli, B. Camisa, G. Barbiera, L. Falcone, A. Purevdorj, M. Genua, F. Sanvito, M. Ponzoni, C. Doglioni, P. Cristofori, C. Traversari, C. Bordignon, F. Ciceri, R. Ostuni, C. Bonini, M. Casucci, A. Bondanza, Monocyte-derived IL-1 and IL-6 are differentially required for cytokine-release syndrome and neurotoxicity due to CAR T cells. *Nat. Med.* **24**, 739–748 (2018).

49. C. Luan, J. Zhou, H. Wang, X. Ma, Z. Long, X. Cheng, X. Chen, Z. Huang, D. Zhang, R. Xia, J. Ge, Case report: Local cytokine release syndrome in an acute lymphoblastic leukemia patient after treatment with chimeric antigen receptor T-cell therapy: A possible model, literature review and perspective. *Front. Immunol.* **12**, 707191 (2021).

50. J. L. Tanyi, C. Stashwick, G. Plesa, M. A. Morgan, D. Porter, M. V. Maus, C. H. June, Possible compartmental cytokine release syndrome in a patient With recurrent ovarian cancer after treatment with mesothelin-targeted CAR-T cells. *J. Immunother.* **40**, 104–107 (2017).

51. J. A. Fraietta, S. F. Lacey, E. J. Orlando, I. Pruteanu-Malinici, M. Gohil, S. Lundh, A. C. Boesteanu, Y. Wang, R. S. O'Connor, W.-T. Hwang, E. Pequignot, D. E. Ambrose, C. Zhang, N. Wilcox, F. Bedoya, C. Dorfmeier, F. Chen, L. Tian, H. Parakandi, M. Gupta, R. M. Young, F. B. Johnson, I. Kulikovskaya, L. Liu, J. Xu, S. H. Kassim, M. M. Davis, B. L. Levine, N. V. Frey, D. L. Siegel, A. C. Huang, E. J. Wherry, H. Bitter, J. L. Brogdon, D. L. Porter, C. H. June, J. J. Melenhorst, Determinants of response and resistance to CD19 chimeric antigen receptor (CAR) T cell therapy of chronic lymphocytic leukemia. *Nat. Med.* **24**, 563–571 (2018).

52. L. Li, V. Mohanty, J. Dou, Y. Huang, P. P. Banerjee, Q. Miao, J. G. Lohr, T. Vijaykumar, J. Frede, B. Knoechel, T. J. Laskowski, S. Liang, J. S. Moyes, R. Nandivada, R. Basar, M. Kaplan, M. Daher, E. Liu, Y. Li, S. Acharya, P. Lin, M. Shanley, H. Rafei, D. Marin, S. Mielke, R. E. Champlin, E. J. Shpall, K. Chen, K. Rezvani, Loss of metabolic fitness drives tumor resistance after CAR-NK cell therapy and can be overcome by cytokine engineering. *Sci. Adv.* **9**, eadd6997 (2023).

53. R. H. Y. Louie, C. Cai, J. Samir, M. Singh, I. W. Deveson, J. M. Ferguson, T. G. Amos, H. M. McGuire, K. Gowrishankar, T. Adikari, R. Balderas, M. Bonomi, M. Ruella, D. Bishop, D. Gottlieb, E. Blyth, K. Micklethwaite, F. Luciani, CAR+ and CAR− T cells share a

differentiation trajectory into an NK-like subset after CD19 CAR T cell infusion in patients with B cell malignancies. *Nat. Commun.* **14**, 7767 (2023).

54. C. Lamarche, K. Ward-Hartstonge, T. Mi, D. T. S. Lin, Q. Huang, A. Brown, K. Edwards, G. E. Novakovsky, C. N. Qi, M. S. Kobor, C. C. Zebley, E. W. Weber, C. L. Mackall, M. K. Levings, Tonic-signaling chimeric antigen receptors drive human regulatory T cell exhaustion. *Proc. Natl. Acad. Sci. U.S.A.* **120**, e2219086120 (2023).

55. H. Wang, R. A. Sica, G. Kaur, P. M. Galbo, Z. Jing, C. D. Nishimura, X. Ren, A. Tanwar, B. Etemad-Gilbertson, B. Will, D. Zheng, D. Fooksman, X. Zang, TMIGD2 is an orchestrator and therapeutic target on human acute myeloid leukemia stem cells. *Nat. Commun.* **15**, 11 (2024).

56. A. Titov, Y. Kaminskiy, I. Ganeeva, E. Zmievskaya, A. Valiullina, A. Rakhmatullina, A. Petukhov, R. Miftakhova, A. Rizvanov, E. Bulatov, Knowns and unknowns about CAR-T cell dysfunction. *Cancers* **14**, 1078 (2022).

57. D. Gumber, L. D. Wang, Improving CAR-T immunotherapy: Overcoming the challenges of T cell exhaustion. *EBioMedicine* **77**, 103941 (2022).

58. J. Tan, Y. Jia, M. Zhou, C. Fu, I. J. Tuhin, J. Ye, M. A. Monty, N. Xu, L. Kang, M. Li, J. Shao, X. Fang, H. Zhu, L. Yan, C. Qu, S. Xue, Z. Jin, S. Chen, H. Huang, Y. Xu, J. Chen, M. Miao, X. Tang, C. Li, Z. Yan, D. Wu, L. Yu, Chimeric antigen receptors containing the OX40 signalling domain enhance the persistence of T cells even under repeated stimulation with multiple myeloma target cells. *J. Hematol. Oncol.* **15**, 39 (2022).

59. J. C. Boucher, G. Li, H. Kotani, M. L. Cabral, D. Morrissey, S. B. Lee, K. Spitler, N. J. Beatty, E. V. Cervantes, B. Shrestha, B. Yu, A. Kazi, X. Wang, S. M. Sebti, M. L. Davila, CD28 costimulatory domain-targeted mutations enhance chimeric antigen receptor T-cell function. *Cancer Immunol. Res.* **9**, 62–74 (2021).

60. Q. Deng, G. Han, N. Puebla-Osorio, M. C. J. Ma, P. Strati, B. Chasen, E. Dai, M. Dang, N. Jain, H. Yang, Y. Wang, S. Zhang, R. Wang, R. Chen, J. Showell, S. Ghosh, S. Patchva, Q. Zhang, R. Sun, F. Hagemeister, L. Fayad, F. Samaniego, H. C. Lee, L. J. Nastoupil, N. Fowler, R. Eric Davis, J. Westin, S. S. Neelapu, L. Wang, M. R. Green, Characteristics of anti-CD19 CAR T cell infusion products associated with efficacy and toxicity in patients with large B cell lymphomas. *Nat. Med.* **26**, 1878–1887 (2020).

61. K. A. Hay, L. A. Hanafi, D. Li, J. Gust, W. C. Liles, M. M. Wurfel, J. A. López, J. Chen, D. Chung, S. Harju-Baker, S. Cherian, X. Chen, S. R. Riddell, D. G. Maloney, C. J. Turtle, Kinetics and biomarkers of severe cytokine release syndrome after CD19 chimeric antigen receptor-modified T-cell therapy. *Blood* **130**, 2295–2306 (2017).

62. A. C. Talleur, A. Qudeimat, J.-Y. Métais, D. Langfitt, E. Mamcarz, J. C. Crawford, S. Huang, C. Cheng, C. Hurley, R. Madden, A. Sharma, A. Suliman, A. Srinivasan, M. P. Velasquez, E. A. Obeng, C. Willis, S. Akel, S. E. Karol, H. Inaba, A. Bragg, W. Zheng, S. M. Zhou, S. Schell, M. Tuggle-Brown, D. Cullins, S. L. Patil, Y. Li, P. G. Thomas, C. Zebley, B. Youngblood, C.-H. Pui, T. Lockey, T. L. Geiger, M. M. Meagher, B. M. Triplett, S. Gottschalk, Preferential expansion of CD8+ CD19-CAR T cells postinfusion and the role of disease burden on outcome in pediatric B-ALL. *Blood Adv.* **6**, 5737–5749 (2022).

63. C. J. Turtle, L. A. Hanafi, C. Berger, T. A. Gooley, S. Cherian, M. Hudecek, D. Sommermeyer, K. Melville, B. Pender, T. M. Budiarto, E. Robinson, N. N. Steevens, C. Chaney, L. Soma, X. Chen, C. Yeung, B. Wood, D. Li, J. Cao, S. Heimfeld, M. C. Jensen, S. R. Riddell, D. G. Maloney, CD19 CAR-T cells of defined CD4+:CD8+ composition in adult B cell ALL patients. *J. Clin. Invest.* **126**, 2123–2138 (2016).

64. X. Ren, M. Peng, P. Xing, Y. Wei, P. M. Galbo, D. Corrigan, H. Wang, Y. Su, X. Dong, Q. Sun, Y. Li, X. Zhang, W. Edelmann, D. Zheng, X. Zang, Blockade of the immunosuppressive KIR2DL5/PVR pathway elicits potent human NK cell–mediated antitumor immunity. *J. Clin. Invest.* **132**, e163620 (2022).

65. A. Dobin, C. A. Davis, F. Schlesinger, J. Drenkow, C. Zaleski, S. Jha, P. Batut, M. Chaisson, T. R. Gingeras, STAR: Ultrafast universal RNA-seq aligner. *Bioinformatics* **29**, 15–21 (2013).

66. S. Anders, P. T. Pyl, W. Huber, HTSeq—A Python framework to work with high-throughput sequencing data. *Bioinformatics* **31**, 166–169 (2015).

67. M. I. Love, W. Huber, S. Anders, Moderated estimation of fold change and dispersion for RNA-seq data with DESeq2. *Genome Biol.* **15**, 550 (2014).

68. A. Subramanian, P. Tamayo, V. K. Mootha, S. Mukherjee, B. L. Ebert, M. A. Gillette, A. Paulovich, S. L. Pomeroy, T. R. Golub, E. S. Lander, J. P. Mesirov, Gene set enrichment analysis: A knowledge-based approach for interpreting genome-wide expression profiles. *Proc. Natl. Acad. Sci. U.S.A.* **102**, 15545–15550 (2005).

69. B. Li, C. N. Dewey, RSEM: Accurate transcript quantification from RNA-Seq data with or without a reference genome. *BMC Bioinformatics* **12**, 323 (2011).

70. T. Ozawa, C. D. James, Establishing intracranial brain tumor xenografts with subsequent analysis of tumor growth and response to therapy using bioluminescence imaging. *J. Vis. Exp.* **41**, 1986 (2010).